

**Diffusion in heterogeneous systems studied by
Laser Scanning Confocal Microscopy and
Fluorescence Correlation Spectroscopy**

Dissertation

zur Erlangung des Grades

"Doktor der Naturwissenschaften"

am Fachbereich Chemie, Pharmazie und Geowissenschaften
der Johannes Gutenberg-Universität Mainz

Mikheil Doroshenko
geboren am 31.08.1987
in Tiflis (Georgien)

Mainz – 2013

Dekan: (is given in printed version)

1. Berichtstatter: (is given in printed version)

2. Berichtstatter: (is given in printed version)

Tag der mündlichen Prüfung: (is given in printed version)

Die vorliegende Arbeit wurde im Zeitraum von Oktober 2010 bis Dezember 2013 am Max-Planck-Institut für Polymerforschung, unter der Betreuung von (is given in printed version) angefertigt.

“Life is not a problem to be solved,
but a reality to be experienced.”

-Søren Kierkegaard

ABSTRACT

Understanding and controlling the mechanism of the diffusion of small molecules, macromolecules and nanoparticles in heterogeneous environments is of paramount fundamental and technological importance. The aim of the thesis is to show, how by studying the tracer diffusion in complex systems, one can obtain information about the tracer itself, and the system where the tracer is diffusing.

In the first part of my thesis I will introduce the Fluorescence Correlation Spectroscopy (FCS) which is a powerful tool to investigate the diffusion of fluorescent species in various environments. By using the main advantage of FCS namely the very small probing volume ($<1\mu\text{m}^3$) I was able to track the kinetics of phase separation in polymer blends at late stages by looking on the molecular tracer diffusion in individual domains of the heterogeneous structure of the blend. The phase separation process at intermediate stages was monitored with laser scanning confocal microscopy (LSCM) in real time providing images of droplet coalescence and growth.

In a further project described in my thesis I will show that even when the length scale of the heterogeneities becomes smaller than the FCS probing volume one can still obtain important microscopic information by studying small tracer diffusion. To do so, I will introduce a system of star shaped polymer solutions and will demonstrate that the mobility of small molecular tracers on microscopic level is nearly not affected by the transition of the polymer system to a “glassy” macroscopic state.

In the last part of the thesis I will introduce and describe a new stimuli responsive system which I have developed, that combines two levels of nanoporosity. The system is based on poly-N-isopropylacrylamide (PNIPAM) and silica inverse opals (iOpals), and allows controlling the diffusion of tracer molecules.

ZUSAMMENFASSUNG

Das Verständnis und die Kontrolle des Diffusionsmechanismus kleiner Moleküle, Makromoleküle und Nanopartikel in heterogenen Umgebungen ist von höchst fundamentaler und technologischer Bedeutung. Das Ziel dieser Arbeit ist es zu zeigen, wie durch die Studie der Diffusion einer Markersubstanz in komplexen Systemen Informationen über den Marker selbst und das System in dem er diffundiert erhalten werden können.

Im ersten Teil meiner Arbeit werde ich in die Fluoreszenzkorrelations-spektroskopie (FCS) einführen, die ein mächtigstes Werkzeug zur Untersuchung der Diffusion fluoreszenter Spezies in verschiedenen Umgebungen ist. Durch die Ausnutzung des Hauptvorteils der FCS, nämlich dem sehr kleinen Probenvolumen ($<1\mu\text{m}^3$) war es mir möglich die Kinetik der Phasenseparation in Polymermischungen in späten Stadien durch die Betrachtung der molekularen Markerdiffusion in einzelnen Domänen der heterogenen Struktur der Mischung zu verfolgen. Der Phasenseparationsprozess in Zwischenstadien wurde mit konfokaler Laserrastermikroskopie (LSCM) in Echtzeit betrachtet, aufgenommen wurden Bilder von Tröpfchenkoaleszenz und -wachstum.

In einem weiteren Projekt, das in meiner Arbeit beschrieben wird, werde ich zeigen dass sogar bei Heterogenitäten von Längenskalen kleiner als das FCS Probenvolumen immer noch wichtige mikroskopische Informationen durch die Betrachtung der Diffusion der kleinen Marker erhalten werden kann. Dafür werde ich das System eines sternförmigen Polymers einführen und werde zeigen dass die Mobilität von kleinen molekularen Markern auf mikroskopischer Ebene nahezu nicht vom Übergang des Polymersystems in einen "glasigen" makroskopischen Zustand beeinflusst wird.

Im letzten Teil meiner Arbeit werde ich ein neues, stimulussensitives System einführen und beschreiben, das ich entwickelt habe und das zwei Ebenen von Nanopores vereint. Das System basiert auf Poly-N-isopropylacrylamid (PNIPAM) und inversen Silicaopalen (iOpals) und erlaubt die Kontrolle der Diffusion von Markermolekülen.

Table of content

Abstract/ Zusammenfassung.....	7
Table of contents	9
1. Introduction	13
1.1. Diffusion	13
1.1.1. Theory of diffusion	14
1.1.1.1. Fick's first law	14
1.1.1.2. Fick's second law	17
1.1.2. Random walk theory	18
1.1.2.1. Simplified model	19
1.2. Motivation	22
2. Methods	25
2.1. Confocal Laser Scanning Microscopy	25
2.1.1. Operational Principle	25
2.1.2. Resolution	28
2.1.3. Laser Illumination and Fluorescence	29
2.1.4. LSCM setup used in this work	30
2.2. Fluorescence correlation spectroscopy (FCS)	31
2.2.1. Introduction to FCS	31
2.2.2. Principle of FCS	32
2.2.3. Autocorrelation function	34
2.2.3.1. Autocorrelation Function for single species	34
2.2.3.2. Autocorrelation Function for multiple species	35
2.2.4. Fluorescence excitation/emission spectra. Jablonski diagram	36

2.2.5. Fluorescent Dyes	39
2.2.6. FCS Setup Used in this work	42
2.3. Scanning electron microscopy (SEM)	42
2.4. Vertical deposition (VD) method	43
2.5. Polymer grafting methods	44
2.5.1. “Grafting-from”	44
2.5.2. “Grafting-to”	45
2.5.3. Atom transfer radical polymerization (ATRP)	46
3. Dynamics of phase separation in a polymer blend	51
3.1. Introduction and Motivation	51
3.2. Materials	52
3.2.1. Sample preparation	52
3.2.2. Annealing process	54
3.3. Phase Diagram and Phase separation by LSCM	54
3.4. Kinetics of the phase separation	59
3.5. Purity of domains	62
3.6. Conclusion	68
4. Dynamics in glassy star shaped polymer solutions	69
4.1. Introduction and motivation	69
4.2. Materials and samples	71
4.3. Tracer diffusion in colloidal star polymer solution	73
4.4. Conclusion	79
5. Temperature controlled diffusion in PNIPAM modified Silica Inverse Opals	81
5.1. Introduction and motivation	81

5.2. Material and sample preparation	83
5.2.1. Silica inverse Opals	83
5.2.1.1. Preparation via Vertical Deposition method	83
5.2.1.2. Modification via ATRP	86
5.2.1.2.1. Materials	86
5.2.1.2.2. Initiator Immobilization	86
5.2.1.2.3. Surface-Initiated Polymerizations	87
5.3. Tracer diffusion in Modified iOpals	89
5.4. Temperature dependent diffusion	92
5.5. Conclusion	94
6. Summery & conclusion	97
Acknowledgments	99
List of symbols	101
List of abbreviations	103
Publications	104
References	105
Curriculum Vitae	112

CHAPTER 1

Introduction

1.1. Diffusion

Diffusion is a process which we meet in a daily life. As an example, if we put a droplet of ink without stirring at the bottom of a bottle filled with water, the color will slowly spread through the whole bottle. Firstly, it will be concentrated near the bottom. After a few days, it will penetrate upwards a few centimeters. And after several days, the solution will be colored homogeneously. The process responsible for the movement of the colored material is diffusion. Diffusion is caused by the Brownian motion of atoms or molecules that leads to complete mixing. In case of gases, diffusion progresses at a rate of centimeters per second; in case of liquids, its rate is typically fractions of millimeters per second, and in case of solids, diffusion is a fairly slow process and the rate of diffusion decreases strongly with decreasing temperature: near the melting temperature of a metal a typical rate is about one micrometer per second; near half of the melting temperature it is only of the order of nanometers per second.

The science of diffusion in solids had its beginnings in the 19th century, although the blacksmiths and metal artisans of antiquity already used the phenomenon to make such objects as swords of steel, gilded copper or bronze wares. Diffusion science is based on several corner stones. The most important ones are: (i) The continuum theory of diffusion originated from work of the German scientist *Adolf Fick*, who was inspired by elegant experiments on diffusion in gases and of salt in water performed by *Thomas Graham* in Scotland. (ii) The Brownian motion was detected by the Scottish botanist *Robert Brown*. He observed small particles

suspended in water migrating in an erratic fashion. This phenomenon was interpreted decades later by *Albert Einstein*. He realized that the ‘movement’ described by *Brown* was a random walk driven by the collisions between particles and the water molecules. His theory provided the statistical cornerstone of diffusion and bridged the gap between mechanics and thermodynamics. It was verified in beautiful experiments by the French Nobel laureate *Jean Baptiste Perrin*. Equally important was the perception of the Russian and German scientists *Jakov Frenkel* and *Walter Schottky* that point defects play an important role for properties of crystalline substances, most notably for those controlling diffusion and the many properties that stem from it.

1.1.1. Theory of diffusion

The equations describing diffusion processes are Fick’s laws. Firstly the work of Adolf Fick appeared in 1855 [1] and described a salt-water system undergoing diffusion. The concept of the diffusion coefficient was introduced, and in addition Fick suggested a linear response between the concentration gradient and the mixing of salt and water.

Fick’s laws describe the diffusive transport of matter as an empirical fact without claiming that it derives from basic concepts. It is, however, indicative of the power of Fick’s continuum description that all subsequent developments have in no way affected the validity of his approach. A deeper physical understanding of diffusion in solids is based on random walk theory which is treated later in this chapter.

1.1.1.1 Fick’s First Law

Let us first consider the flux of diffusing particles in one dimension (x-direction) like shown in Figure 1.1. The particles can be atoms, molecules, or ions.

Fick's first law for an isotropic medium can be written as:

$$J_x = -D \frac{\partial C}{\partial x} \quad (1.1)$$

Here J_x is the flux of particles (diffusion flux) and C their number density (concentration). The negative sign in equation indicates opposite directions of the diffusion flux and concentration gradient. Diffusion is a process which leads to an equalisation of concentration. The factor of proportionality, D , is denoted as the diffusion coefficient or as the diffusivity of the species considered.

Units: The diffusion flux is expressed in number of particles (or moles) traversing a unit area per unit time and the concentration in number of particles per unit volume. Thus the diffusivity D has the dimension of *length² per time* and bears the units [$\text{cm}^2 \text{s}^{-1}$] or [$\text{m}^2 \text{s}^{-1}$].

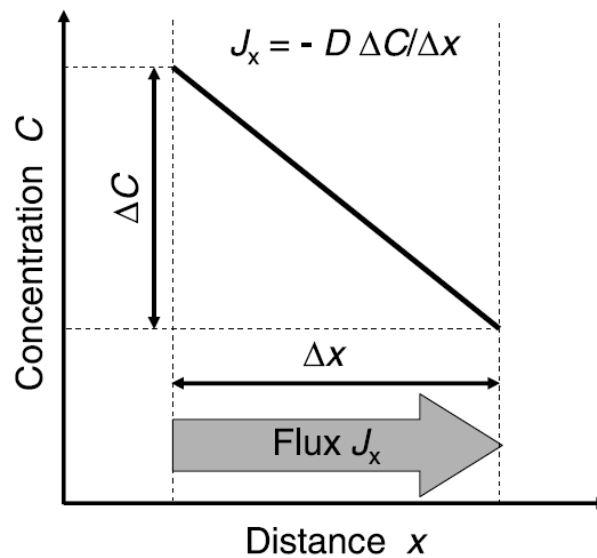


Figure 1.1. Illustration of Fick's first law

Fick's first law is easily generalized to three dimensions using a vector notation:

$$J = -D \nabla C \quad (1.2)$$

The vector of the diffusion flux J is directed opposite in direction to the concentration gradient vector ∇C . The *nabla* symbol, ∇ , is used to express the vector operation on the right-hand side. The nabla operator acts on the scalar concentration field $C(x, y, z, t)$ and produces the concentration-gradient field ∇C . The concentration-gradient vector always points in that direction for which the concentration field undergoes the most rapid increase and its magnitude equals the maximum rate of increase of concentration at the point. For an isotropic medium the diffusion flux is antiparallel to the concentration gradient.

Usually, in diffusion processes the number of diffusing particles is conserved. Let us choose an arbitrary point P located at (x, y, z) and a test volume of size Δx , Δy , and Δz (Figure 1.2).

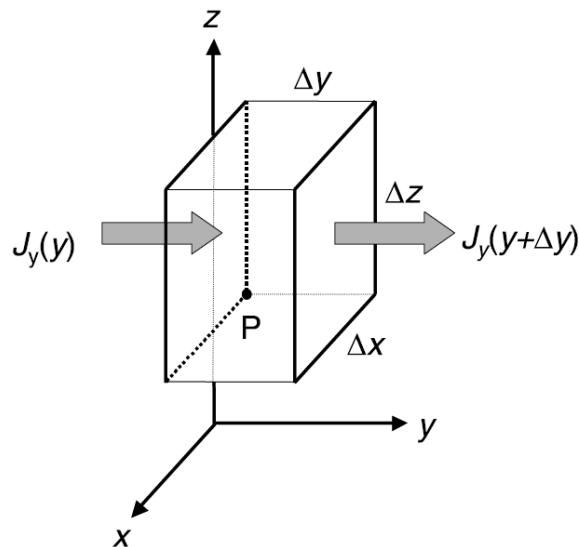


Figure 1.2. Infinitesimal test volume. The in- and outgoing y-components of the diffusion flux are indicated by arrows.

The diffusion flux J and its components J_x, J_y, J_z vary across the test volume. If the sum of the fluxes leaving and entering the test volume do not balance, a net accumulation (or loss) must occur. This material balance can be expressed as

$$\text{inflow} - \text{outflow} = \text{accumulation (or loss) rate.}$$

The flux components can be substituted into this equation to yield

$$\begin{aligned} & [J_x(P) - J_x(P + \Delta x)]\Delta y\Delta z + \\ & [J_y(P) - J_y(P + \Delta y)]\Delta x\Delta z + \\ & [J_z(P) - J_z(P + \Delta z)]\Delta x\Delta y = \text{accumulation (or loss) rate.} \end{aligned}$$

Using Taylor expansions of the flux components up to their linear terms, the expressions in square brackets can be replaced by $\Delta x\partial J_x/\partial x$, $\Delta y\partial J_y/\partial y$, and $\Delta z\partial J_z/\partial z$, respectively. This yields:

$$-\left[\frac{\partial J_x}{\partial x} + \frac{\partial J_y}{\partial y} + \frac{\partial J_z}{\partial z}\right]\Delta x\Delta y\Delta z = \frac{\partial C}{\partial t}\Delta x\Delta y\Delta z \quad (1.3)$$

where the accumulation (or loss) rate in the test volume is expressed in terms of the partial time derivative of the concentration. For infinitesimal size of the test volume, Equation (1.3) can be written in compact form by introducing the vector operation *divergence* ∇ , which acts on the vector of the diffusion flux:

$$-\nabla \cdot J = \frac{\partial C}{\partial t} \quad (1.4)$$

1.1.1.2 Fick's Second Law

By combination of above mentioned equations, we can get the following:

$$\frac{\partial C}{\partial t} = \nabla \cdot (D \nabla C) \quad (1.5)$$

From the mathematical point of view Fick's second law is a second-order partial differential equation. It is non-linear if D depends on concentration, which is, for example, the case when diffusion occurs in a chemical composition gradient. The composition-dependent diffusivity is usually denoted as the *interdiffusion coefficient*. If the diffusivity is independent of concentration, which is the case for tracer diffusion in chemically homogenous systems or for diffusion in ideal solid solutions, the equation above can be simplified to:

$$\frac{\partial C}{\partial t} = D \nabla^2 C \quad (1.6)$$

where Δ denotes the *Laplace operator*. This form of Fick's second law is sometimes also called the *linear diffusion equation*. It is a linear second-order partial differential equation for the concentration field $C(x, y, z, t)$. One can strive for solutions of this equation, if boundary and initial conditions are formulated.

1.1.2. Random Walk Theory

From a microscopic point of view, diffusion occurs by the *Brownian motion* of atoms or molecules. As already mentioned above, Albert Einstein in 1905 [2] published a theory for the chaotic motion of small particles suspended in a liquid. Einstein argued that the motion of these particles is due to the presence of molecules in the fluid. He further pointed that molecules due to their Boltzmann distribution of energy are always subject to thermal movements of a statistical nature. According to Einstein stochastic motions occur in matter all the way down to the atomic scale. He related the mean square displacement of particles to the diffusion coefficient. The

same relation was developed nearly the same time by the Polish scientist Smoluchowski. [3, 4] Nowadays it is called the *Einstein relation* or the *Einstein-Smoluchowski relation*.

In gases, diffusion occurs by free flights of atoms or molecules between their collisions. The individual path lengths of these flights are distributed around some well-defined mean free path. Diffusion in liquids exhibits more subtle atomic motion than gases. Atomic motion in liquids can be described as randomly directed shuffles, each much smaller than the average spacing of atoms in a liquid. Most solids are crystalline and diffusion occurs by atomic hops in a lattice, due to many individual displacements (jumps) of the diffusing particles. Diffusive jumps are usually single-atom jumps of fixed lengths, the size of which is of the order of the lattice parameter. Jump processes are promoted by thermal activation. Usually an Arrhenius law holds for the jump rate Γ :

$$\Gamma = \nu^0 \exp\left(-\frac{\Delta G}{K_B T}\right) \quad (1.7)$$

The prefactor ν^0 denotes an attempt frequency of the order of the Debye frequency of the lattice. ΔG is the Gibbs free energy of activation, K_B the Boltzmann constant, and T the absolute temperature. Details can be found in a review by Haenggi et al. [5] and in the textbook of Flynn. [6]

1.1.2.1. Simplified model

Before going through more rigorous mathematical solutions of random walks, it may be helpful to look at a simple situation: unidirectional diffusion of interstitials in a simple cubic crystal. Let us assume that the diffusing atoms are dissolved in low concentrations and that they move by jumping from an interstitial site to a

neighboring one with a jump length λ as demonstrated in Figure 1.3. We suppose a concentration gradient along the x -direction and introduce the following definitions:

Γ : jump rate (number of jumps per unit time) from one plane to the neighboring one,

n_1 : number of interstitials per unit area in plane 1,

n_2 : number of interstitials per unit area in plane 2.

Without a driving force, forward and backward hops occur with the same jump rate and the net flux J from plane 1 to 2 is

$$J = \Gamma n_1 - \Gamma n_2 \quad (1.8)$$

The quantities n_1 and n_2 are related to the volume concentrations (number densities) of diffusing atoms via

$$C_1 = \frac{n_1}{\lambda}, \quad C_2 = \frac{n_2}{\lambda} \quad (1.9)$$

Usually in diffusion studies the concentration field, $C(x, t)$, changes slowly as a function of the distance variable x in terms of interatomic distances. From a Taylor expansion of the concentration-distance function, keeping only the first term (Figure 1.3), we get

$$C_1 - C_2 = -\lambda \frac{\partial C}{\partial x} \quad (1.10)$$

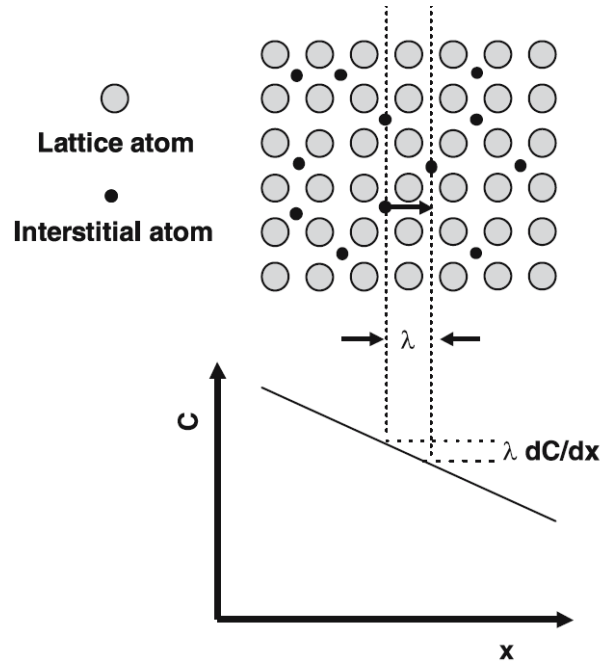


Figure 1.3. Schematic representation of unidirectional diffusion of atoms in a lattice

Inserting Equations (1.9) and (1.10) into Eq. (1.8) we get

$$J = -\lambda^2 \Gamma \frac{\partial C}{\partial x} \quad (1.11)$$

By comparison with Fick's first law we obtain for the diffusion coefficient

$$D = \Gamma \lambda^2 \quad (1.12)$$

Taking into account that in a simple cubic lattice the jump rate of an atom to one of its six nearest-neighbor interstices is related to its total jump rate via $\Gamma_{\text{tot}} = 6\Gamma$, we obtain:

$$D = \frac{1}{6} \Gamma_{tot} \lambda^2 \quad (1.13)$$

This equation shows that the diffusion coefficient is essentially determined by the product of the jump rate and the jump distance squared.

1.2. Motivation

As we saw from previous subchapter, diffusion is not a simple process even when relatively simple homogeneous systems are considered. On other hand, understanding the mechanism of the diffusion of small molecules, macromolecules and nanoparticles in complex, nanostructured environments is of paramount fundamental and technological importance. Indeed, diffusion is often the dominant mechanism for the transport of such species in e.g. solid nano-porous structures, polymer solutions and gels or living cells. Thus, it is relevant for many processes and applications including drug delivery, cell nutrition, porous chromatography, polymer synthesis and separation, treatment of waste water, oil recovery, mineral processing, drying of paints, production of personal care products, etc. Not surprisingly therefore, studying the penetrant diffusion and correlating it to the chemical, physical and topological characteristics of the nanostructured environment had become a major research topic in various fields spanning from polymer physics to cell biology. A number of theories, models and empirical relations have been introduced to describe the diffusion of small species in polymer systems, in intercellular matrices or in solid periodic nano-porous structures.

During last decades a lot of techniques have been developed to study diffusion process. Mostly used ones are: pulse-field-gradient NMR (PFG-NMR), forces Rayleigh scattering (FRS), dynamic light scattering (DLS), fluorescence

recovery after photobleaching (FRAP), etc. [7-9]. All the mentioned technics have specific advantages but also some limitations. For example they may require relatively high concentration of the tracer to enhance signal to noise ratio, however the local properties might significantly change due to high amount of these tracers. In addition the main disadvantage of these techniques is the large probing volume and thus the lack of ability to address the local dynamics in heterogeneous systems, which may be of crucial importance.

Recently Fluorescence Correlation Spectroscopy (FCS) has emerged as a powerful tool to investigate the diffusion of fluorescent molecules, macromolecules or nanoparticles in various environments. Detailed description on working principle of FCS is given in chapter 2. For decades FCS has been limited mostly to biological studies, i.e. aqueous environments. [10-15] Only recently FCS was successfully applied to study the size and conformation of macromolecules in organic solvents [16, 17], in gels [18, 19], in polymer solutions and melts [20-25] and polymer blends [26].

By studying the diffusion of the small molecules in different systems, first one obtains information about the molecule itself: how it is diffusing in different environment, does it have any interaction with the system, what forces drive this molecule to diffuse and so on. Second, information about the properties of the system in which the molecule is diffusing can be obtained: i.e. the viscosity, the length scale of the possible heterogeneities, does system change its properties in time.

In my thesis I will describe both above mentioned phenomena. In the chapter 3 I will show, how by using FCS and studying the diffusion of small tracer molecules one can obtain information about the local properties of the environment and thus track the phase separation kinetics in polymer blend. Here the very small probing volume of the FCS ($<1\mu\text{m}^3$) allows looking in individual domains of a heterogeneous structure. In chapter 4 I will demonstrate that even when the length scale of the heterogeneities becomes smaller than the FCS probing volume one can still obtain

important microscopic information by studying small tracer diffusion. To this end I will introduce a system of star shaped polymer solutions and show that the mobility of small molecular tracers on microscopic level, is almost unaffected by the transition of the polymer system to a “glassy” macroscopic state. Finally, in chapter 5, I go beyond simply monitoring the diffusion, and describe the design of a system that combines two levels of nanoporosity and allows control of the diffusion of tracer molecules.

CHAPTER 2

Methods

2.1. Confocal Laser Scanning Microscopy

The confocal microscope was invented by Marvin Minsky [27] in 1957 at Harvard University. The lateral resolution it offers is only slightly improved in comparison to conventional wide field fluorescence microscopy. However, what really sets the confocal microscope apart from its wide field counterpart is its far superior axial resolution, allowing thin sections through a sample to be imaged.

In addition the confocal microscope allows almost all out of focus fluorescence to be omitted. This greatly improved image contrast and quality. Figure 2.1 (Images taken from [28]) below shows a comparison of wide field and confocal images.

Combined with improvements in laser technology, the confocal microscope has allowed imaging of living samples that could not have been imaged by conventional optical microscopy or electron microscopy. It has been also utilized in multi-disciplinary sciences to study photo-luminescence [29] in semi-conductor films, bioluminescent interaction with nanoparticles. [30] In the pharmaceutical industry, it was recommended to follow the manufacturing process of thin film pharmaceutical forms, to control the quality and uniformity of the drug distribution. [31]

2.1.1. Operational Principle

The improvements gained by the confocal microscope arise from its system of illumination and detection of fluorescence. In comparison to wide field

fluorescence microscopy where the entire field of view is illuminated, excitation in the confocal microscope is achieved by point illumination.

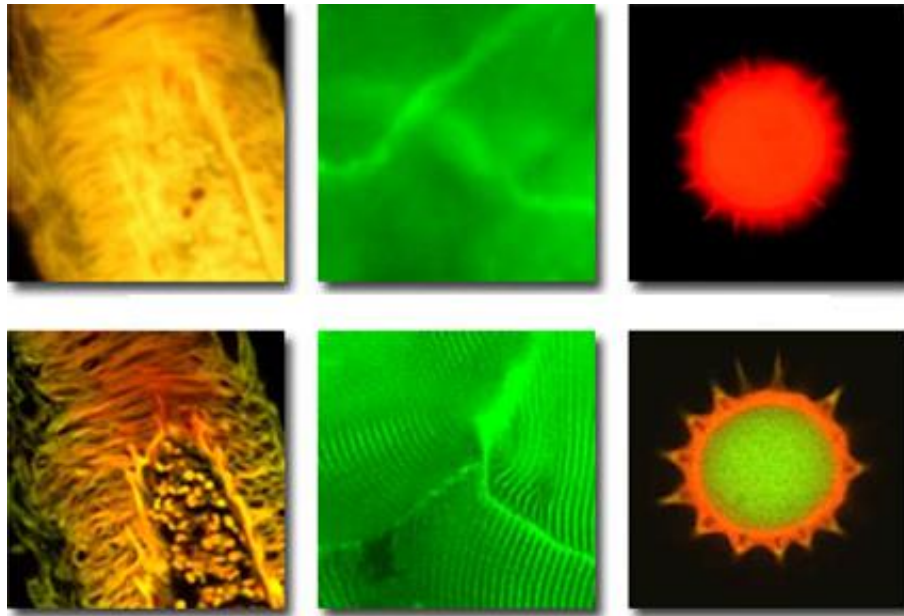


Figure 2.1. Top: Images acquired in wide field mode. Bottom: A single section acquired in confocal mode showing the increased image detail achievable when the out of focus background is eliminated.

Typically a laser beam is tightly focused by a microscope objective to a diffraction limited focal spot and this spot is raster scanned across the sample (Figure 2.2). [28]

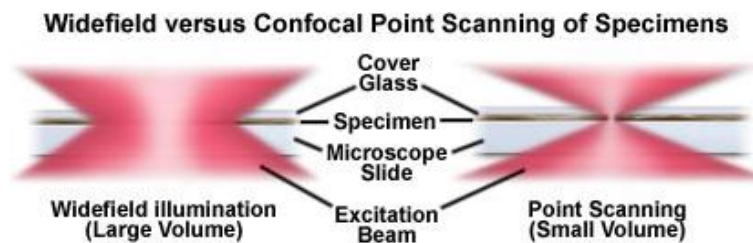


Figure 2.2. Illustration of confocal excitation and widefield illumination of a fluorescent sample.

The created fluorescence light is collected by the same objective and guided to a fast and sensitive detector, typically photo multiplier or avalanche photo diode. Additionally, in order to insure the small size of the probing volume also in normal direction, a small ($\sim 100 \mu\text{m}$) pinhole is placed in the image plane in front of the detector. Thus almost all the fluorescence that is generated out of the focal plane is eliminated. It can be seen that only the in focus light from the excitation spot passes through the detection pinhole. Light from below/above the focal plane comes to a focus before/after the detection pinhole (Figure 2.3). [28]

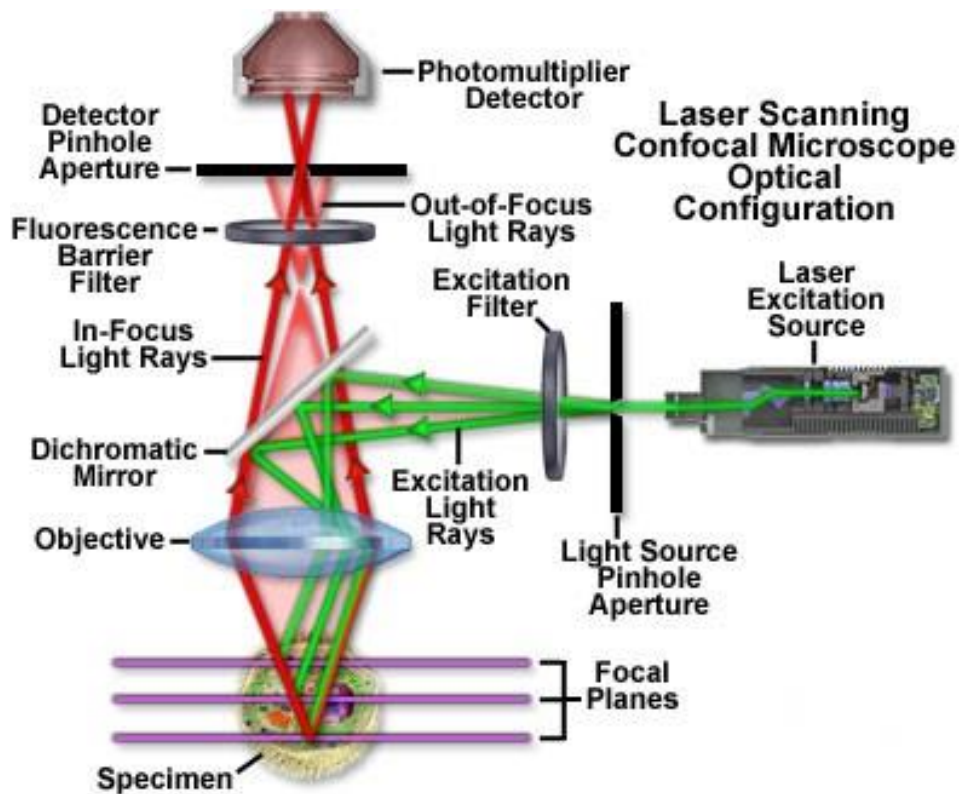


Figure 2.3. Illustration of principle of operation of a confocal microscope.

2.1.2. Resolution

The confocal microscope is an optical microscope and therefore its resolution is limited by diffraction. This means a point source is not imaged to a single point in the image plane. There are many definitions of resolution in use in optical microscopy. Qualitatively it is the minimum separation of two point sources which can still be distinguished [30]. The size of the spot that is formed in the image plane is governed by the wavelength of the light, λ , and the numerical aperture (NA) of the lens. The NA is calculated from (2-1) and is governed by the semi-angle α and the refractive index of the medium, n .

$$NA = n \cdot \sin \alpha \quad (2.1)$$

Due to the diffraction of the light with conventional means one cannot achieve lateral size of the observation volume smaller than roughly half of the wavelength of the light used [32]

$$r_0 = 1.22 \frac{\lambda}{2NA_{obj}} \quad (2.2)$$

In addition, in axial direction resolution is much worse [32]

$$z_0 = \frac{1.5n\lambda}{NA_{obj}^2} \quad (2.2)$$

where λ – wavelength of the light, NA_{obj} – numerical aperture of the objective, n – refractive index of the medium.

2.1.3. Laser Illumination and Fluorescence

The laser provides an intense source of light at a specific wavelength. Lasers suitable for confocal microscopy are available in a wide range of wavelengths [29] from near infrared to ultraviolet.

To obtain diffraction limited excitation spot the whole of the back focal aperture of the objective must be uniformly illuminated. Practically this is achieved by expanding the laser beam to completely fill the back focal aperture of the objective. When the beam is the same size as the back focal aperture the objective is said to be fully filled. The laser beam will not have a uniform beam profile though; it is more likely to be approximately Gaussian. [33] By further expanding the beam and only using the central portion a more uniform beam profile is presented to the objective lens, although this is at the expense reduced transmitted light. [30]

The most common and useful imaging mode used in confocal microscopy is the fluorescence mode. Samples are stained or prepared to contain fluorescent tags or molecules.

The major problem with fluorophores is that they fade (irreversibly) when exposed to excitation light (Figure. 8). Although this process is not completely understood, it is believed that it to occur when fluorophore molecules react with oxygen or oxygen radicals and become nonfluorescent. [34-36] The reaction can take place after a fluorophore molecule transitions from the singlet excited state to the triplet excited state. Although the fraction of fluorophores that transitions to the triplet state is small, its lifetime is typically much longer than that of the singlet state. This can lead to a significant triplet state fluorophore population and thus to significant photobleaching. [37] Some strategies have been developed to reduce the rate of photobleaching. [36, 37] One of the approaches is to reduce the amount of oxygen that would react with the triplet excited states. And this can be easily done by displacing it using an inert gas. [37] Another approach is to use the free-radical

scavengers to reduce the oxygen radicals. Shortening the long lifetime of the triplet excited state has also been shown to be effective. [38] Other ways include using a high numerical aperture lens to collect more fluorescence light and thus use less excitation light. [39] Also, keeping the magnification as low as is permissible spreads the excitation light over a larger area, thereby reducing the local intensity. While photobleaching makes fluorescence microscopy more difficult, it is not always undesirable. One technique that takes advantage of it is fluorescence recovery after photobleaching (FRAP). [9] It involves exposing a small region of the specimen to a short and intense laser beam, which destroys the local fluorescence, and then observing as the fluorescence is recovered by transport of other fluorophore molecules from the surrounding region. Quantities such as the diffusion coefficient of the dyed structures can then be determined. [40]

2.1.4. LSCM setup used in this work

Imaging of polymer blends was made with a commercial setup consisting of an inverted microscope (IX70) and a confocal laser scanning unit, FluoView FV300 (Olympus, Japan). Either a PLAPON 60 \times oil immersion objective (1.45 NA, 100 μ m working distance) or a MPLAPO 50 \times dry objective (0.95 NA, 300 μ m working distance) were used, respectively, for the room temperature and elevated temperature studies. The fluorescein dyes attached to the PS chains were excited with the 488 nm line of a 20 mW Argon laser fiber coupled to the laser scanning unit. Fluorescence images were recorded using a LP 505 long-pass emission filter. The microscope cover glasses with the deposited polymer blend samples were mounted in an Attofluor steel chamber (Invitrogen) with the polymer film pointing upwards for the room temperature studies. For studies at elevated temperature the cover glasses were mounted on a THMS 600 heating stage (Linkam) with the polymer film pointing down i.e. towards the microscope objective. The obtained LSCM images were

analyzed using the “imageJ” software package, including the “LOCI” and “Radial Profile” plugins. The same software with appropriate thresholds was used in obtaining the number of grains, their average size and area as a function of time.

2.2. Fluorescence Correlation Spectroscopy (FCS)

2.2.1. Introduction to FCS

FCS was first described in the early 1970s in a series of classic papers. An extensive description and its application can be found in recent publications. [10-19] FCS is based on the analysis of time-dependent intensity fluctuations that are the result of some dynamic process, typically translational diffusion into and out a small observation volume, defined by a focused laser beam and a confocal aperture. When the fluorophore diffuses into a focused light beam, there is a burst of emitted photons due to multiple excitation-emission cycles from the same fluorophore. If the fluorophore diffuses rapidly out of the volume photon burst is short lived. In case of slow diffusion the photon burst displays a longer duration. By correlation analysis of the time-dependent fluctuations of the emission signal, one can determine the diffusion coefficient of the fluorophore.

In addition to translational diffusion, intensity fluctuations can occur due to ligand-macromolecule binding, rotational diffusion, intersystem crossing and excited state reactions. [41-43] Different equations are needed to describe each process, and usually two or more processes affect the data at the same time. Also important is to account for the size and shape of the observation volume. As a result, the theory and equations for FCS are rather complex.

2.2.2. Principle of FCS

On Figure 2.4 schematic drawing of Fluorescence Correlation Spectroscopy setup is presented. The scheme is very similar to that of a confocal microscopy described above. Excitation is usually accomplished with a laser focus to a diffraction-limited spot using high numerical aperture objective. When the fluorescent species enter this spot, they are excited and the emitted fluorescence is collected by the same objective, passing through the dichroic mirror and emission filters. A confocal pinhole is used to reject out of focus signal.

Afterwards, the light is reaching a detector, usually avalanche photodiode (APD) or photomultiplier (PMT) with single photon sensitivity.

Using these optical conditions, an ellipsoidal observation volume is created that is elongated along the optical axis, with the main axis of r_0 and z_0 with the rough size of $0.2 \mu\text{m}$ and $1 \mu\text{m}$ respectively, i.e. with total volume of less than a $1\text{fl}=10^{-15}$ liters. The average number of fluorophores in the volume is determined by their bulk concentration and remains constant in a stationary experiment. If the fluorophore concentration is 1nM (that is a typical value used in experiments), then the observation volume contains less than 0.6 molecules in average. When the

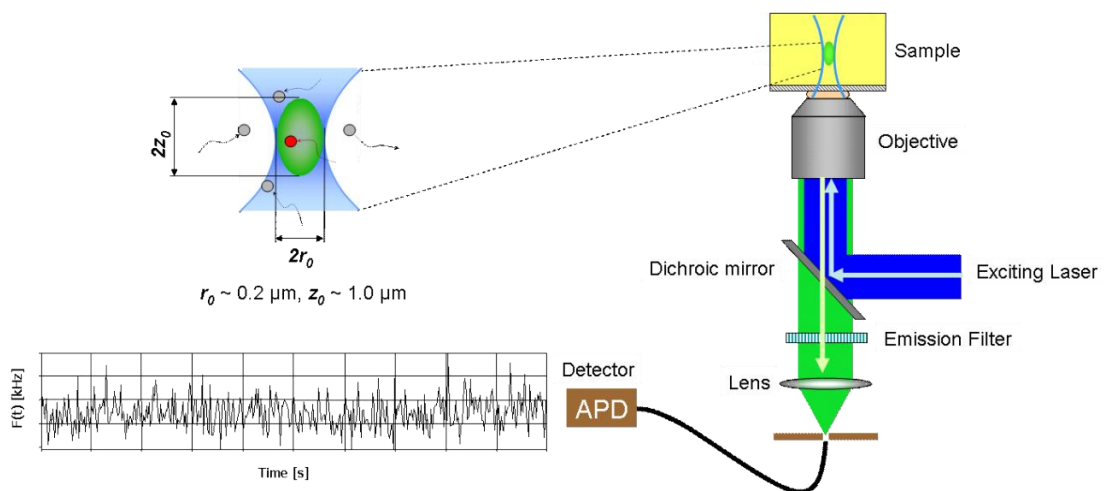


Figure 2.4. Schematic drawing of Fluorescence Correlation Spectroscopy

fluorophores diffuse in and out of the observation volume, they cause fluorescence intensity fluctuations. The intensity at a given time $F(t)$ is compared with the intensity at a given time $F(t+\tau)$. If the diffusion is slow $F(t)$ and $F(t+\tau)$ are likely to be similar. In case of fast diffusion, $F(t)$ and $F(t+\tau)$ are likely to be different.

For obtaining quantitative information about the diffusion process, these fluctuations can be analyzed in terms of fluorescence intensity autocorrelation function (ACF). [44, 45]

The fluorescence intensity autocorrelation function $G(\tau)$ can be expressed by using the fluorescent light intensity fluctuations $\delta F(t)$ as follows:

$$G(\tau) = \frac{\langle F(t) \cdot F(t + \tau) \rangle}{\langle F(t) \rangle^2} \quad 2.3$$

On Figure 2.5 (taken from [46]) it is shown how the autocorrelation curve can be schematically constructed. The brackets $\langle \rangle$ indicate the time average over the fluorescence signal, t is the time at which the fluorescent intensity is recorded and τ is the correlation lag time. The above formula is integrated and normalized: [47, 48]

$$\begin{aligned} G(\tau) &= \frac{\langle [F(t) + \delta F(t)] \cdot [F(t) + \delta F(t + \tau)] \rangle}{\langle F(t) \rangle^2} \\ &= \frac{\langle F(t) \rangle^2 \langle \delta F(t) \cdot \delta F(t + \tau) \rangle}{\langle F(t) \rangle^2} \\ &= 1 + \frac{\langle \delta F(t) \cdot \delta F(t + \tau) \rangle}{\langle F(t) \rangle^2} \end{aligned} \quad 2.4$$

Where $\delta F(t) = F(t) - \langle F(t) \rangle$, because $\delta F(t)$ gives the corresponding fluorescent fluctuations in the fluorescent signal $F(t)$ around the mean value $\langle F(t) \rangle$. And $\langle \delta F(t) \cdot \langle \delta F(t) \rangle \rangle = \langle \langle \delta F(t) \rangle \cdot \delta F(t) \rangle = 0$, since $\langle \delta F(t) \rangle = 0$

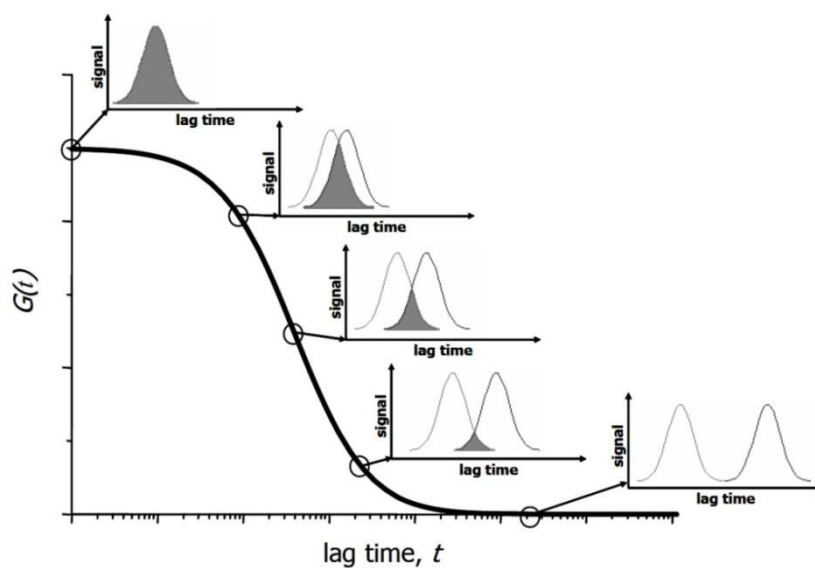


Figure 2.5. Schematic representation of autocorrelation curve formation in the lag time, t , in Fluorescence Correlation Spectroscopy

2.2.3. Autocorrelation function

In order to extract information, such as concentration, diffusion coefficient, reaction rate constant, from the measured autocorrelation functions one has to fit it with a theoretical correlation function. There are several reviews concerning the theories of the autocorrelation functions. [45, 49-51]

2.2.3.1 Autocorrelation function for single type of species

Autocorrelation function $G(\tau)$ for single type of fluorescent species with diffusion coefficient D and molar concentration c is: [49]

$$G(\tau) = 1 + \frac{1}{c \cdot V_{eff}} \frac{1}{\left(1 + \frac{4D\tau}{\omega_0^2}\right)} \frac{1}{\sqrt{1 + \frac{4D\tau}{z_0^2}}} \quad 2.5$$

where V_{eff} is the effective observation volume, which depends on the geometry of the focus for excitation and emission. Commonly it is approximated with 3 dimensional Gaussian profile with ω_0 and z_0 are the half-widths in x-y plane and in the z direction, respectively. These parameters can be obtained from calibration measurements with a solution of fluorophores having known diffusion coefficient. By putting average particle number $N = c \cdot V_{eff}$, the effective diffusion time $\tau_D = \omega_0^2/4D$, and the structure parameter $k = \omega_0/z_0$ in the equation above, we will get:

$$G(\tau) = 1 + \frac{1}{N} \frac{1}{\left(1 + \frac{\tau}{\tau_D}\right)} \frac{1}{\sqrt{1 + \frac{\tau}{k^2\tau_D}}} \quad 2.6$$

The diffusion coefficient D is related to the size of the fluorescent molecules via the Stokes-Einstein equation:

$$D = \frac{kT}{6\pi\eta R} \quad 2.7$$

Where k is the Boltzmann constant, T is the absolute temperature, η is the viscosity of the medium and R is the hydrodynamic radius of the molecule.

2.2.3.2 Autocorrelation function for multiple types of species

In case of several types of noninteracting fluorescent species diffusing in the observation volume with different diffusion coefficients, the fluorescence intensity

autocorrelation function is the sum of the contributions of the individual species. The $G(\tau)$ for the mixture of m of different fluorescent species is given by:

$$G(\tau) = 1 + \frac{1}{N} \sum_{i=1}^m p_i g_i(\tau) \quad 2.9$$

Where $g_i(\tau) = \frac{1}{\left(1 + \frac{\tau}{\tau_{Di}}\right)} \frac{1}{\sqrt{1 + \frac{\tau^2}{k^2 \tau_{Di}^2}}}$ and $p_i = \frac{\phi_i^2 c_i}{\sum_{i=1}^m \phi_i^2 c_i}$

In the equation above, p_i is the relative amplitude of the molecules with distinct diffusion coefficients, c_i is the concentration of these molecules and ϕ_i is the fluorescent brightness of species i . [52]

2.2.4 Fluorescence excitation and emission spectra. Jablonski diagram

Fluorescence is the emission of photons by atoms or molecules whose electrons are transiently stimulated to a higher excitation state by radiant energy from an outside source. When a fluorescent molecule absorbs a photon of the appropriate wavelength, an electron is excited to a higher energy state and almost immediately returns back to its initial ground state. In the process of energy collapse the molecule can release the absorbed energy as a fluorescent photon. Since some energy is lost in the process, the emitted fluorescent photon typically exhibits a lower frequency of vibration and a longer wavelength than the excitatory photon that was absorbed. This can be graphically illustrated in Figure 2.6., and is known as a Jablonski diagram. Jablonski diagrams are often used as the starting point for discussion light absorption and emission. To illustrate various molecular processes that can occur in excited states. The diagrams are named after Professor Alexander Jablonski, who is regarded

as the father of fluorescence spectroscopy because of his many accomplishments, including description of concentration depolarization and defining the term “anisotropy” to describe the polarized emission from solutions.

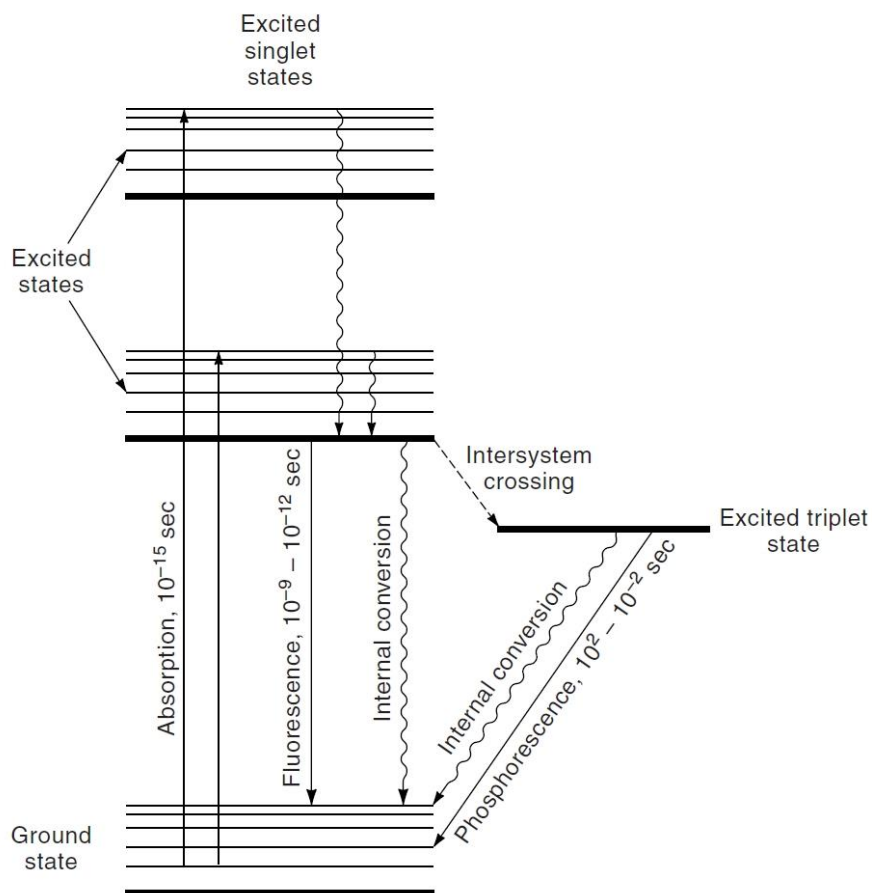


Figure 2.6. Jablonski diagram showing energy levels occupied by an excited

There are two categories of excited states - the singlet excited state and the triplet excited state. Most commonly, an excited electron occupies an excitation level within the singlet excited state, and when it returns to the ground state, energy can be given up as fluorescence emission. Alternatively, energy can be given up as heat (internal conversion), in which case no photon is emitted. When excited above the ground state, there is also a probability that an electron enters the triplet excited state.

Molecules with electrons in this state are chemically reactive, which can lead to photobleaching and the production of damaging free radicals.

In case of *fluorescence*, the absorption and re-emission events occur nearly simultaneously, within the interval of 10^{-9} – 10^{-12} seconds; therefore, fluorescence stops the moment there is no more exciting incident light. There is also possibility that the period between excitation and emission lasts longer and can take from a second to minutes; such emission process is called *phosphorescence*.

Molecules that are capable of fluorescing are called *fluorescent molecules*, *fluorescent dyes*, or *fluorochromes*. Fluorochromes exhibit distinct excitation and emission spectra that depend on their atomic structure and electron resonance properties. Molecules absorb light and re-emit photons over a spectrum of wavelengths (the *excitation spectrum*) and exhibit one or more characteristic excitation maxima (Figure 2.7.)

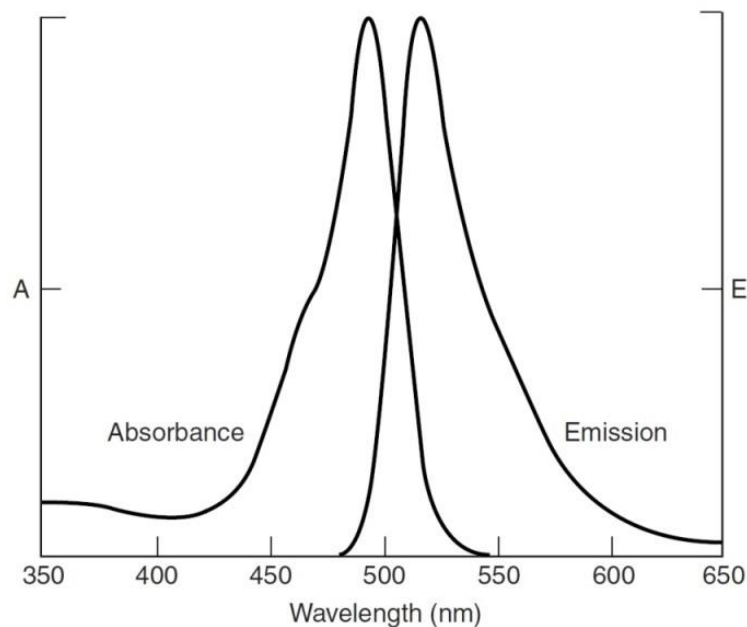


Figure 2.7. Normalized absorption and fluorescence emission spectra of fluorescent dye.

Absorption and excitation spectra are distinct but usually overlap, sometimes to the extent that they are nearly indistinguishable. However, for many fluorescent dyes like Fluorescein, Alexa, Rhodamine, the absorption and excitation spectra are clearly distinct. The widths and locations of the spectral curves are important, particularly when selecting two or more fluorochromes for labeling different molecules within the same specimen.

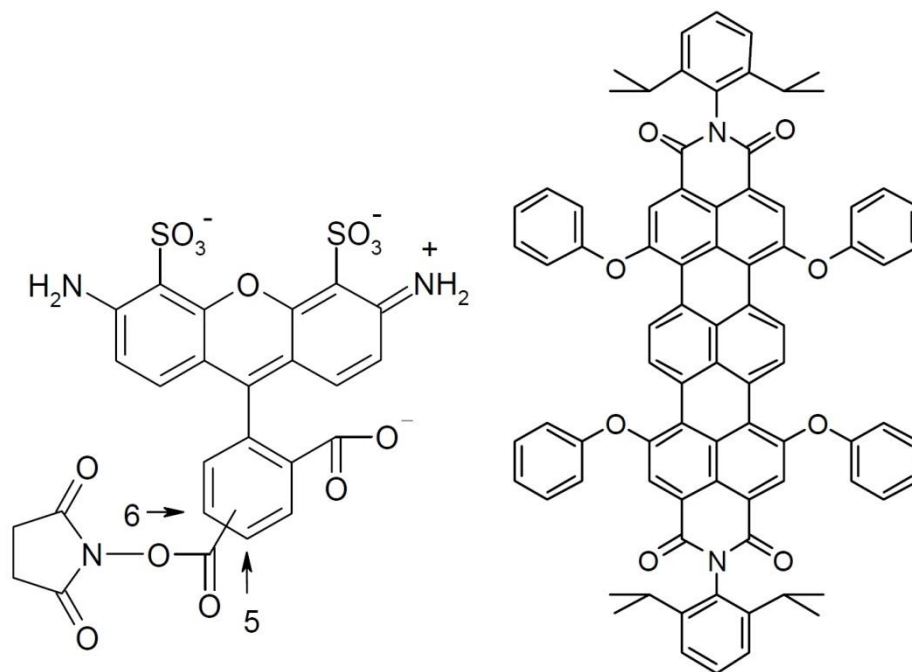
Finally, the shapes of spectral curves and the peak wavelengths of absorption and emission spectra vary, depending on factors contributing to the chemical environment of the system, including pH, ionic strength, solvent polarity, O₂ concentration, presence of quenching molecules, and others. This fact explains why the fluorescence of a dye such as fluorescein varies depending on whether it is free in solution or conjugated to a protein or other macromolecule.

2.2.5. Fluorescent Dyes

Initially FCS measurements were done by using fluorophores that are already known from fluorescence spectroscopy and microscopy techniques. [53] As described above FCS is a single molecule technique and the high quantum efficiency, large absorption cross section and photostability are the key requirements of fluorophores for such techniques. For aqueous systems Fluorescein and Alexa dye family exhibits a large selection of different colors with absorption maxima ranging from 350 nm to 750 nm, covering more than the visible spectrum. For the non-aqueous systems, chromospheres which are dissolved in organic solvents are usually used. Such are rylene family dyes. Because of the very good photostability and high quantum yield [54, 55] they are suitable dyes for the FCS studies.

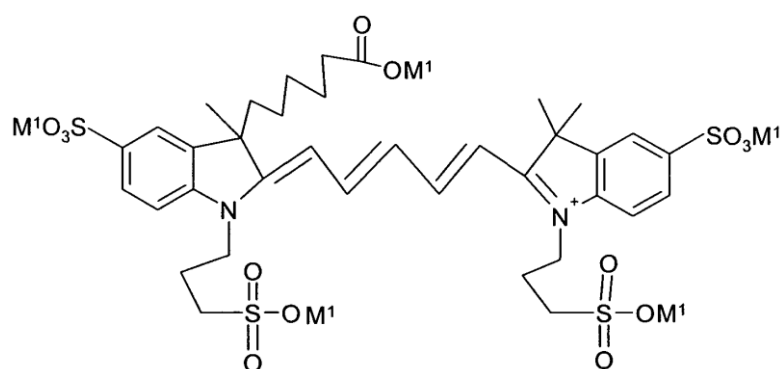
In this work I used in-house synthesized N, N'-bis(2,6-Diisopropylphenyl)-1,6,9,14-tetrahydroxyterrylene-3,4:11,12-tetracarboxy-diimide, a terrylene (TDI) dye, to study the dynamics of the phase separation process in polymer blends and also to study mobility of the small tracer in glassy star-shaped polymer solutions. In one of the

projects I used the commercially available Alexa Fluor 488 and Alexa Fluor 647 (Invitrogen, Karlsruhe, Germany) to study the diffusion in PNIPAM modified Silica Inverse Opals. The chemical structures of the dyes are given in Figure 2.8.



(b) Alexa Fluore 488

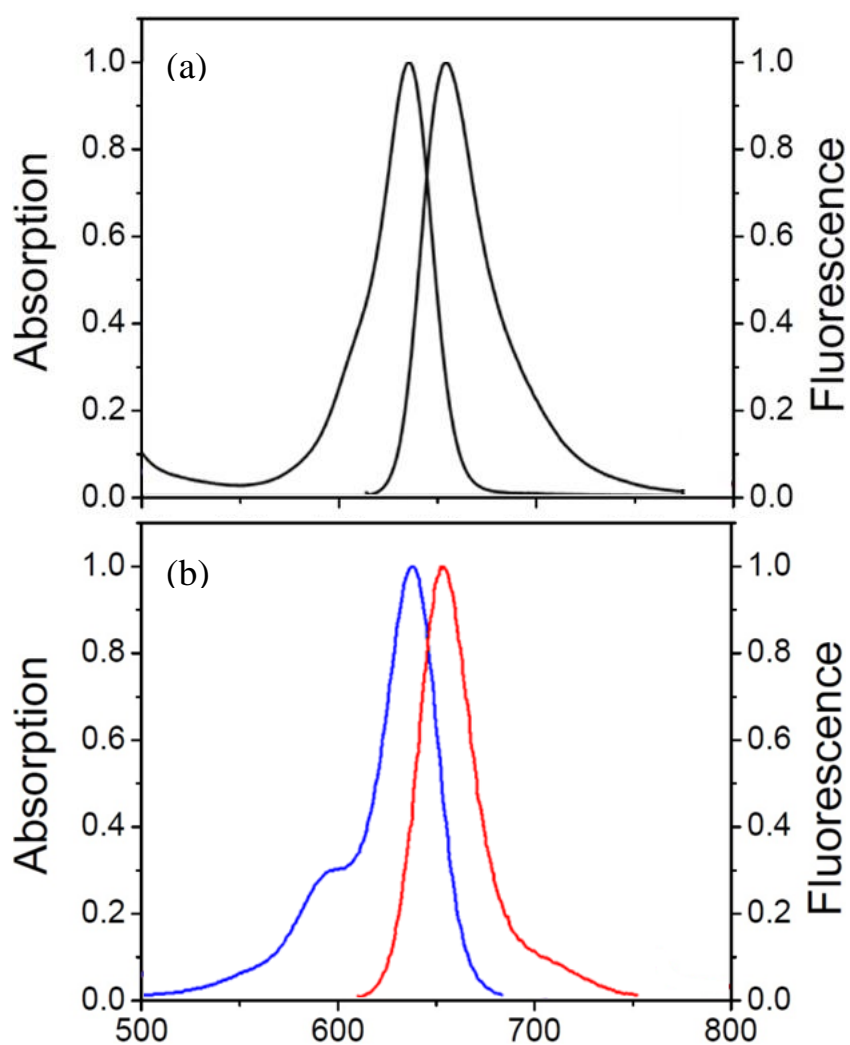
(a) Terrylene (TDI)



(c) Alexa Fluore 647

Figure 2.8. Molecular structure of the fluorescent dyes (a) Alexa Fluore 488, (b) Terrylene (TDI), (c) Alexa Fluore 647

In FCS experiment Alexa Fluor 488 dyes were excited with a 488 nm Argon laser and the emission filter LP488R was used to collect the fluorescence. The Alexa Fluor 647 and the Terrylene (TDI) dyes were excited with the 633-nm line of a Helium-Neon laser. Emission was collected after filtering through a LP635R long-pass filter. Adsorption and emission spectra of the mentioned fluorescent dyes are given in Figure 2.9



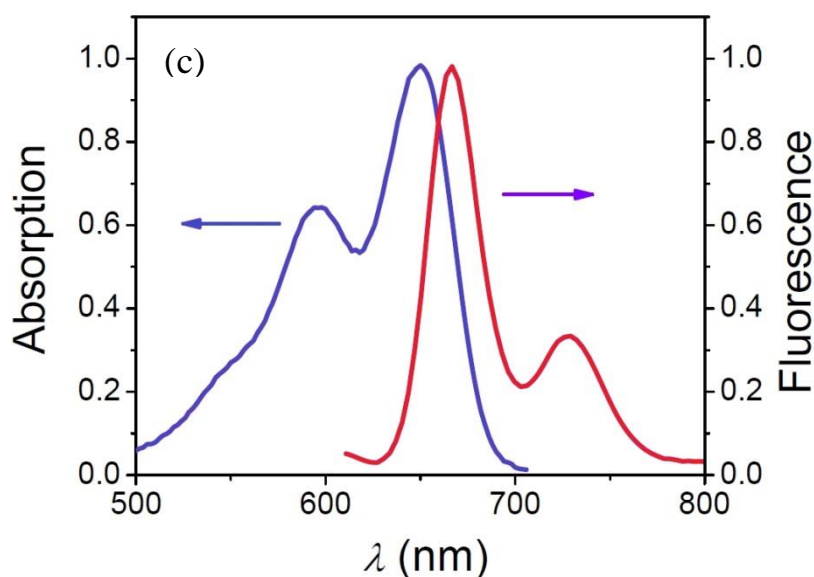


Figure 2.9. Absorption and fluorescent emission spectra of the following dyes (a) Alexa Fluore 488, (b) Alexa Fluore 647, (c) Terrylene (TDI)

2.2.6. FCS Setup used in this work

The FCS measurements were performed on a commercial setup based on the Olympus laser scanning confocal microscope described in (2.1.4) that was extended with a fiber coupled FCS unit (Pico Quant, Germany). For the studies of the inverse opals filled with aqueous solutions, a 60x water immersion objective with numerical aperture of 1.2 and 200 μm working distance was used. Since the inverse opal layer was a relatively thin film with some cracks and defects, a LSCM was performed prior to the FCS measurement to identify appropriate position of the inverse opal layer. At each position a series of 10 measurements with a total duration 5 min was performed.

2.3. Scanning electron microscopy (SEM)

In scanning electron microscopy (SEM), an electron beam is used to map the

surface of a specimen. [56, 57] An electron beam with energy of few keV is emitted by a cathode (gun) and focused by condenser lenses. The beam is used to scan a rectangular area of the specimen line-by-line. The electrons interact with the atoms at or near the sample surface depending on the acceleration voltage. Back-scattered or secondary electrons are detected by specialized detectors. This signal is amplified and yields a magnified black and white image of the sample surface with resolutions in the nm range (and below). Different grey scale values in the SEM image arise from differences in the electron densities of the materials. Elements of higher atomic number appear brighter than those of lower atomic number.

2.4. Vertical deposition (VD) method

The assembly of colloids into well-defined structures occurs under the influence of external fields, e.g., gravitational sedimentation, [58] electrophoretic deposition, [59] or vertical deposition either by evaporation [60] or lifting the substrate. [61] In the vertical lifting deposition method when a hydrophilic substrate is immersion into a colloidal dispersion a meniscus is formed at substrate water interface. At the three phases contact lines (air, dispersion, and substrate) evaporation takes place and this causes a solvent flux towards the meniscus, as shown in Figure 2.10.

Thus, colloidal particles are constantly transported with the liquid to the crystallization front. An interplay of long-range attractive and short-range repulsive forces causes the self-assembly of the colloidal material into a face-centered cubic or hexagonally close packed crystal. [62, 63]

In order to control the thickness of such a colloidal crystal, some parameters should be optimized. The substrate is withdrawn from the dispersion at a certain speed at given at curtain temperature and humidity.

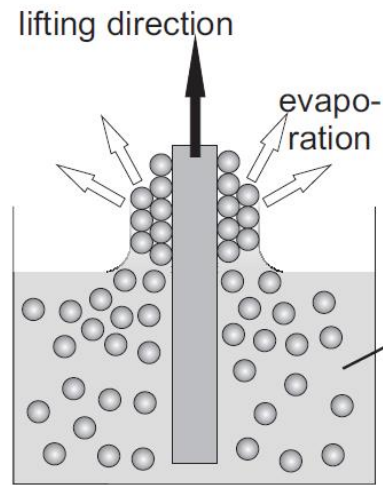


Figure 2.10. Schematic draw of the colloidal crystallization process in a vertical lifting deposition apparatus.

Alongside with this research, also the counterpart to the highly ordered crystals - colloidal glasses [64] - comprising of two distinct, monodisperse latex particles have already been developed. [65] Doping of the colloidal crystal with removable moieties (sacrificial templates) opens a pathway to the designed introduction of defects, which are highly interesting with respect to their contribution to phononic properties. At the same time, colloidal crystals and glasses serve as templates for the fabrication of so-called inverse opals. [66] These materials exhibit a highly ordered interconnected 3D network with high surface area, since the constituent spheres of the colloidal crystals have been removed.

2.5. Polymer grafting methods

2.5.1. “Grafting-from”

In a “grafting-from” approach a polymer brushes are obtained by “growing”

the polymer away from the surface (Figure 2.11a). This is usually done using an initiator functionalized surface and polymerization of the monomer on top of the surface. There are numerous polymerization methods working in this way. [67, 68] In recent years “grafting-from”-techniques using living radical polymerization, especially ATRP (Chapter 2.4.3), have become popular. This is due to the ability to obtain grafted polymers with narrow molecular weight distributions and straightforward experimental procedures. [68-71]

The biggest advantage of the "grafting-from" technique is the very high grafting density of the obtained polymer brushes. During the polymerization the already polymerized monomer is swollen by the monomer/solvent solution. This allows the monomer to freely diffuse to the growing chain end and continue the reaction. Only at high grafting densities and molecular weight distributions the diffusion gets hindered and the polymerization is stopped.

2.5.2. “Grafting-to”

In a “grafting-to” approach a polymer brushes are obtained by attaching an already polymerized chain with certain molecular weight to a surface (Figure 2.11b).

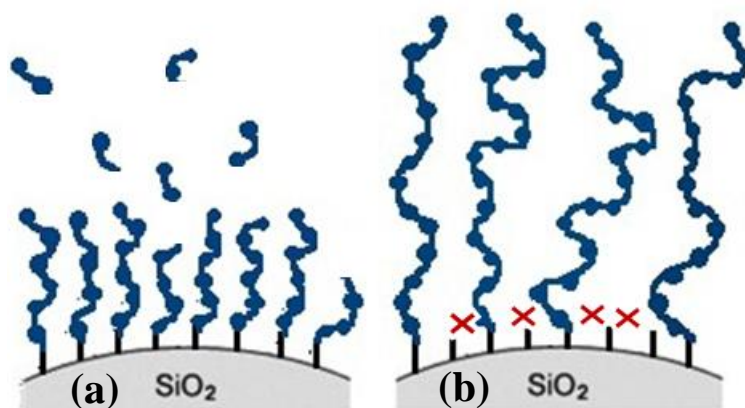


Figure 2.11. Schematic representation of the “grafting-from”(a) and “grafting-to”

To do so, mostly a functionalized polymer is attached to a surface carrying a complimentary functional group. The biggest advantages are the simple synthesis and characterization of the used polymers.

Typically, the used polymers are obtained by living polymerization techniques by using either a functionalized starter or stopping the polymerization with a specific reactant, the end-functionalization is achieved. The consecutive “grafting-to” step can be performed in solution or melt, where usually higher grafting densities are obtained. Compared to the “grafting-from” approach only polymer brushes with lower grafting densities are achieved.

2.5.3. Atom transfer radical polymerization (ATRP)

The free radical polymerization is one of the most important polymerization techniques used for production of high molecular weight polymers. [70, 71] A variety of different monomers can be suited for this type of polymerization and copolymerization under certain experimental conditions. Typically, the free radical polymerization can be done in a high temperature range between the room temperature and 100 °C under ambient pressure. The polymerization can be carried out in organic solution, aqueous media or in solvent mixture. In contrast to the step-growth polymerization, high molecular weight products are obtained already after short reaction times and at low conversions. While the most kinds of alkenes functionalized with hydroxy-, amino- and acid- groups can be used, nearly 50 % of all commercial polymers are produced by the free radical polymerization. The most known examples for commercially synthesized polymers via radical polymerization are ethylene, styrene, vinyl chloride and (meth) acrylates.

One should also mention that the control over the molecular weight and the polydispersity of the products is difficult as a result of chain transfer and termination reactions between radicals. While the chain transfer reactions can be suppressed by

the proper choice of reaction conditions, the diffusion driven termination of the free radicals, namely recombination and disproportionation, can hardly be avoided. In order to minimize the termination reactions and to obtain the polymers with high molecular weights, the concentration of radicals is minimized to some ppm. However still the rate of initiation is much lower than the rate of propagation, thus, the number of growing chains is very small during the polymerization (~0.1 %). And this leads to a broad distribution of the chain lengths, and the preparation of polymers with controlled architecture is not possible using the free radical polymerization.

Controlled living radical polymerization techniques such as *atom transfer radical polymerization* (ATRP) [70, 72] allows the synthesis of high molecular weight polymers of well-defined architecture in the absence of chain transfer or termination reactions. In ATRP a controlled radical polymerization is achieved by a dynamic equilibrium between an active and a dormant species. The fundamental steps involved in ATRP are shown in Figure 2.12. The basic mechanism of ATRP is the reversible, homolytic cleavage of an alkyl halide R-X by a transition metal complex L_nM_z .

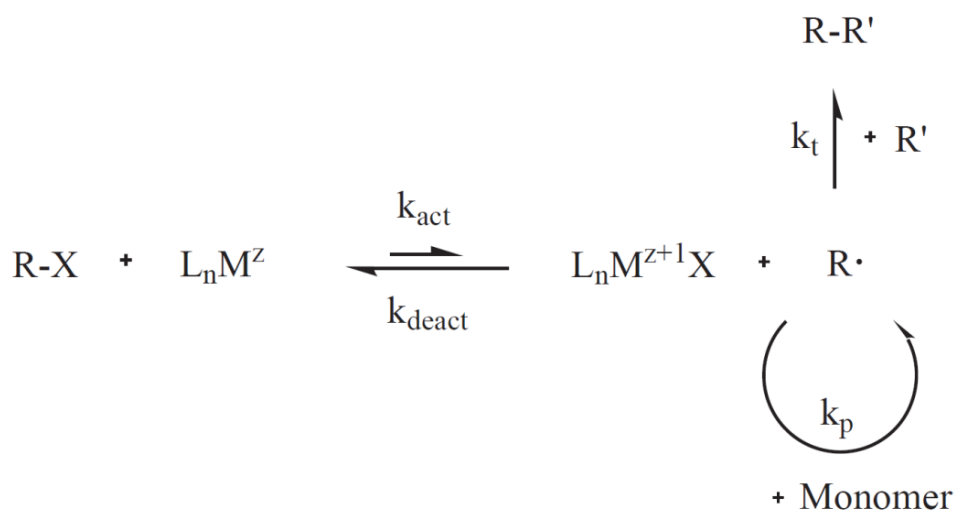


Figure 2.12. Schematic representation of the mechanism of ATRP

The transition metal is oxidized, and an alkyl radical is generated. Similar to the free radical polymerization, the generated radical can attach a monomer or undergo radical-radical termination. However, in ATRP the rate constant of deactivation k_{deact} is much higher than the rate constant of activation k_{act} , favoring the dormant species rather than the active radical. Thus, by trapping the radical in the dormant form, which cannot undergo recombination, the radical concentration is reduced. Thus, the rate constant of termination k_t is significantly reduced compared to the rate constant of propagation k_p , and termination reactions are almost completely avoided. After a certain time in the dormant state, the polymer chain is reactivated and more monomer can be added. The active species reacts with only a few monomer units before it is converted back into the dormant form. Thereby, each polymer chain is active for only a few milliseconds and stays in the dormant state for several seconds. Typically, in a polymerization this cycle is repeated 1000 times, and a total lifetime of several hours is achieved. As a result the lifetime of a polymer chain is significantly increased compared to the free radical polymerization where a growing polymer chain adds monomer every 1 millisecond and has a lifetime of only 1 second. Additionally, in ATRP the initiation is much faster than in the free radical polymerization, and all chains are essentially initiated at the same time. For this reason all the chains grow to identical length, and the product with the low polydispersity ($1.0 < M_w/M_n < 1.5$) is obtained. The degree of polymerization X can be adjusted by the initial monomer to initiator ratio:

$$X = \frac{[M]_0}{[I]_0}$$

After the polymerization the chains remain active allowing their end-functionalization and the synthesis of copolymers by sequential monomer addition.

ATRP can be conducted in a wide temperature range from sub-zero to > 100 °C. The list of monomers suitable for ATRP includes styrenes, (meth) acrylates, (meth) acrylamides, acrylonitrile, vinylpyridine and others. Transition metals like Fe, Ni, Co are used to mediate the reaction. However, the best results are obtained using copper catalysts which allows processing of various monomers in a number of different solvents. Polydentate, N-containing ligands like alkylamines and pyridines are used to mediate ATRP. [73-75] The ligands increase the solubility of the copper complex in organic solvents and adjust the atom transfer equilibrium. Usually the chemical structure of the initiator is similar to the one of the monomer.

CHAPTER 3

Dynamics of phase separation in a polymer blend

3.1. Introduction and Motivation

Spinodal decomposition (SD) [76-80] is widespread phenomenon occurring in diverse systems: from metallic alloys, to glasses, ceramics, fluid mixtures, surfactant micellar solutions and in polymer mixtures. The latter are considered as model systems in studying phase separation kinetics. This is mainly due to their long characteristic times that allow studying *in situ* their morphology.

Ideally, one would like to explore the details of the phase separation process *in situ* monitoring grain nucleation, dissolution, approach of domains, coalescence, and growth within the different regimes. In addition, microscopic information on the interfacial width and of the local composition within the domains is essential.

Apart from different scattering techniques, laser scanning confocal microscopy (LSCM) has emerged as a powerful tool in studying the morphology of such heterogeneous systems. LSCM is a non-destructive method and has strong depth discrimination that is achieved by proper use of a confocal pinhole in the image plane. In such configuration only light coming from the focal point is detected and out-of-focus light is rejected thus the images are practically optical sections. As a result, image processing allows for a 3D visualization of the exact morphology. With respect to the latter, earlier efforts provided 3D images of bicontinuous polymer blends obtained via SD. [81-86] Subsequent studies tested the calculated structure factor against the measured one via scattering experiments and found an excellent agreement. [82, 83] Further LSCM studies in polymer blends include *in situ* monitoring the shrinkage of the mixtures during the photo-polymerization process,

[87] the blend surface morphology [88] and the protein-polymer co-localization in a phase separated polymer blend. [89]

The aim of the present investigation is twofold. First, to monitor the phase separation process of a polymer blend in real time with LSCM, and second, to obtain independent information on the purity of phases. For the latter, LSCM is coupled to fluorescence correlation spectroscopy (FCS).

The chosen system is a polystyrene/poly(methyl phenyl siloxane) (PS/PMPS) blend. The blend phase separates upon lowering the temperature, thus exhibits an upper critical solution temperature or UCST. In addition it possesses large dynamic asymmetry as revealed by the difference between the component glass temperatures, $\Delta T_g \sim 113$ K at $P=0.1$ MPa. The phase behavior has been investigated experimentally and theoretically both at ambient pressure [90, 91] and more recently at elevated pressures. [92] In addition, the glass temperature, T_g , of the hard phase (PS), interferes with the demixing process thus giving rise to pinning of the domain structure at a certain stage. Specific information on the degree of purity of phases was provided by probing the dynamics at the segmental level by dielectric spectroscopy (DS). [92]

3.2 Materials

3.2.1. Sample Preparation

Direct visualization of the phase separation in the PS/PMPS blends using LSCM requires fluorescent labeling of one of the polymers. Fluorescein labeled polystyrenes with different molecular weights, PS-12k ($M_w=12.2$ kg/mol) and PS-2k ($M_w=2.2$ kg/mol) were purchased from Polymer Standards Service (PSS, Mainz, Germany) and were further purified via precipitation in methanol in order to remove any remaining not covalently attached fluorescein molecules. After purification the

samples were characterized by Gel Permeation Chromatography (PS was used as a standard, THF as an eluent) that yielded molecular weights and polydispersities that are shown in Table 3.1. Poly(methylphenyl siloxane) (PMPS) with molecular weight $M_w=2.27$ kg/mol was synthesized in house following synthesis and purification strategy described previously. [93]

M_w, PS (g/mol)	N_{PS}	M_w/M_n (PS)	$M_w, PMPS$ (g/mol)	N_{PMPS}	M_w/M_n (PMPS)
12200	116	1.17	2270	16	1.67
2230	21	1.20			

Table 2.1. Molecular Characteristics of the Homopolymers

Thin films of symmetric PS/PMPS blends (**Table 2.2**) on microscope cover glasses were prepared as follows. First, the PS and PMPS were independently dissolved in toluene and then mixed, e.g. 0.02g of PS in 1g of toluene + 0.02g of PMPS in 1g toluene. The mixture was stirred for 7-8 h at room temperature. Films were prepared by casting the blended solution on round microscope cover glasses with diameter of 25 mm and thickness of 0.15 mm.

Blend	N_{PS}	N_{PMPS}	w_{PS}
PS ₁₁₆ /PMPS ₁₆	116	16	0.50
PS ₂₁ /PMPS ₁₆	21	16	0.50

Table 2.2. Molecular characteristics of the blends

Since the thickness of the film should be relatively high to minimize surface effects on morphology, most of the toluene was evaporated prior casting, i.e. final amount of mixture

$\approx 0.1 - 0.2$ g. The casted films were dried at ambient condition overnight and for further 48 h in vacuum at 50°C.

3.2.2. Annealing Process

To follow the phase separation kinetics different specimens from the same blend were annealed under vacuum at various temperatures (from 60 to 140°C) and for various times (from 30 min up to 24 h) and then quenched to ambient temperature and studied by LSCM.

For the FCS studies films containing a terylene dye, N,N'-bis(2,6-diisopropylphenyl)-1,6,9,14-tetraphenoxy-terrylene-3,4,11,12-tetra-carboxidiimide (TDI) were prepared by adding an appropriate amount of a 10^{-8} M toluene solution of the dye to the polymer mixture.

3.3. Phase Diagram and Phase separation by LSCM

The type of morphology in polymer blends (spherical or fibrillar dispersed phase vs. co-continuous phases), depends not only on the volume fraction but also on the viscosity and elasticity of the components as well as processing conditions. [76-78, 94] The phase diagram of the studied PS₁₁₆/PMPS₁₆ blend is shown in Figure 3.1.

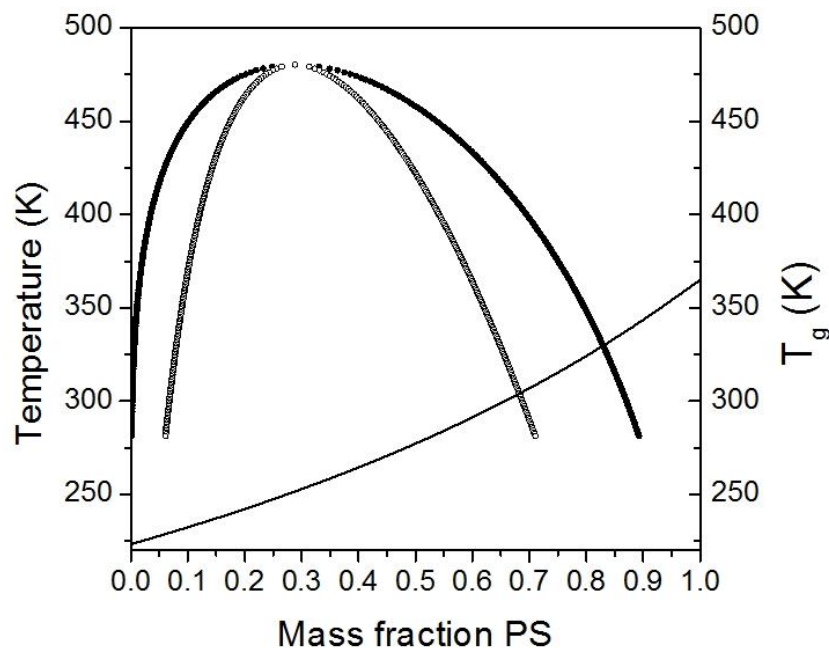


Figure 3.1. Model phase diagram corresponding to the experimental PS₁₁₆/PMPS₁₆ blend. Both the bimodal (filled symbols) and the spinodal (open symbols) curves are shown. The solid line is the theoretical Fox equation.

The PS/PMPS theoretical phase diagram was successfully tested earlier against experimental data for different symmetric PS/PMPS blends. [96] The type of morphology in polymer blends (spherical or fibrillar dispersed phase vs. co-continuous phases), depends not only on the volume fraction but also on the viscosity and elasticity of the components as well as processing conditions. [87, 88, 90]

The symmetric PS₁₁₆/PMPS₁₆ blend shows clear signs of phase separation. Figure 3.2. shows a series of LSCM images from different specimens of the blend that were annealed at 120°C for different time intervals. In all images the green and black domains correspond to PS- and PMPS-rich domains, respectively.

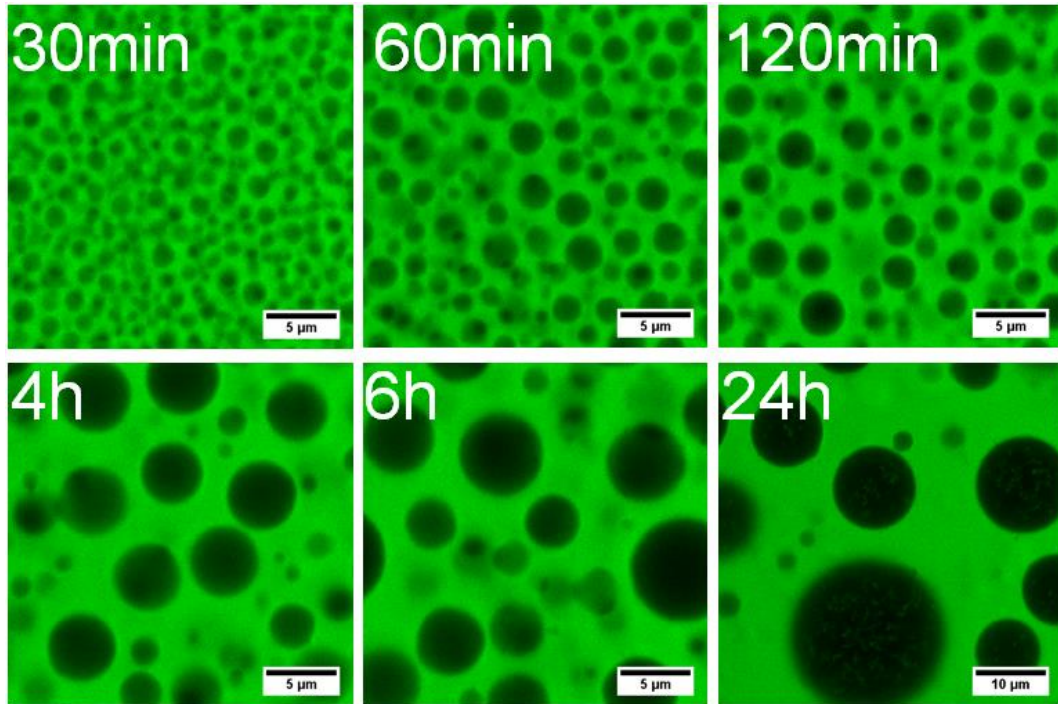


Figure 3.2. Confocal fluorescence microscopy images showing the effect of annealing time on phase separation of the PS₁₁₆/PMPS₁₆ blend. Annealing was made at 120°C and the corresponding annealing time is given in left upper corners. The green area corresponds to fluorescein labeled PS-rich regions, and the dark regions to the unlabeled PMPS-rich regions.

At 120°C the symmetric blend is located within the 2-phase region and is well-above the glass temperature of a PS homopolymer with the same degree of polymerization as the PS in the blend ($T_g^{\text{PS}} = 92^\circ\text{C}$). Following this annealing procedure all specimens were quenched to ambient temperature and imaged. At this temperature the PS-domains are glassy thus restricting the domain growth. For the shortest annealing time ($t = 30 \text{ min}$) the morphology consists of a broad distribution of dark spherical domains of the PMPS-rich phase embedded in a continuous PS-rich matrix. With increasing annealing time the larger PMPS-rich domains grow at the expense of smaller ones and the final distribution resembles more to a bimodal

distribution. In addition, the final annealing temperature has a strong effect on the domain growth. The PMPS-rich domains become larger with increasing annealing temperature that indicates a diffusion controlled process (Figure 3.3)

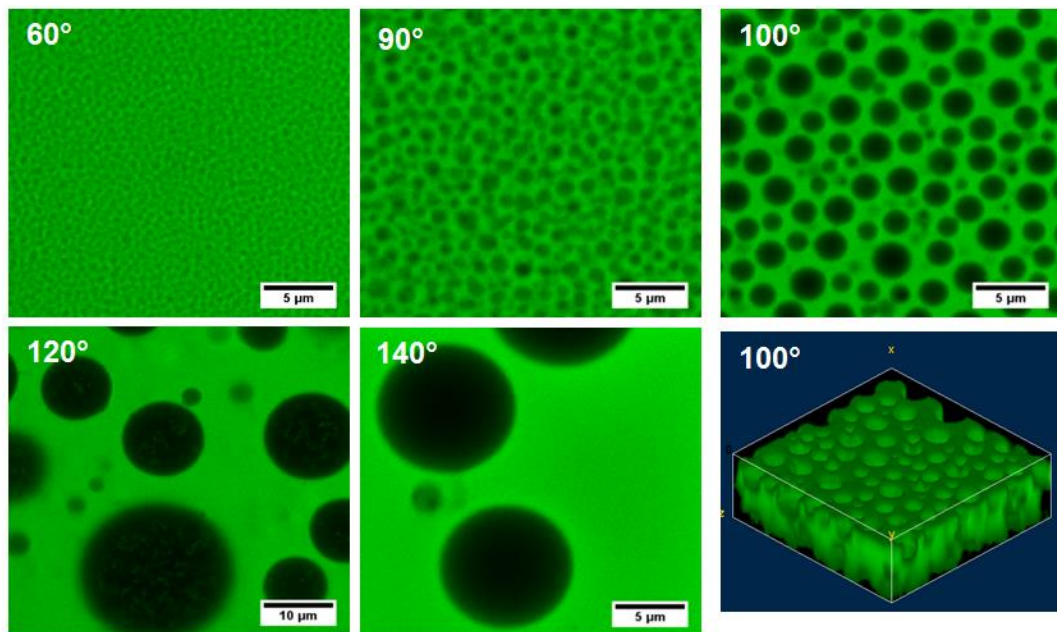


Figure 3.3. Confocal fluorescence microscopic images showing the effect of annealing temperature on the phase separation of the PS₁₁₆/PMPS₁₆ blend. All specimens were annealed for 24 hours at temperatures indicated in the left upper corners. Images were recorded at room temperature. A three-dimensional image reconstruction corresponding to the specimen annealed at 100°C is also shown.

The dark domains grow even when annealed at 90°C, i.e., few degrees below the glass temperature of bulk PS. This suggests that the PS matrix includes some fraction of PMPS (i.e. faster) chains. Indeed, earlier dielectric relaxation experiments [21] on the symmetric blend PS₄₈/PMPS₁₇ revealed a PS-rich phase with PS

composition of volume fraction $\phi_{\text{PS}}^{\text{PS-rich}} = 0.67$. This indicates that the matrix phase in the LSCM images is actually a mixture of slow PS with some faster PMPS chains

In addition the blend containing lower molecular weight PS, PS₂₁/PMPS₁₆ was also prepared and annealed according to the procedure mentioned above. In Figure 3.4 LSCM images showing the effect of annealing temperature are given. Blends are microscopically homogeneous at room temperature, independently of the annealing temperature and time.

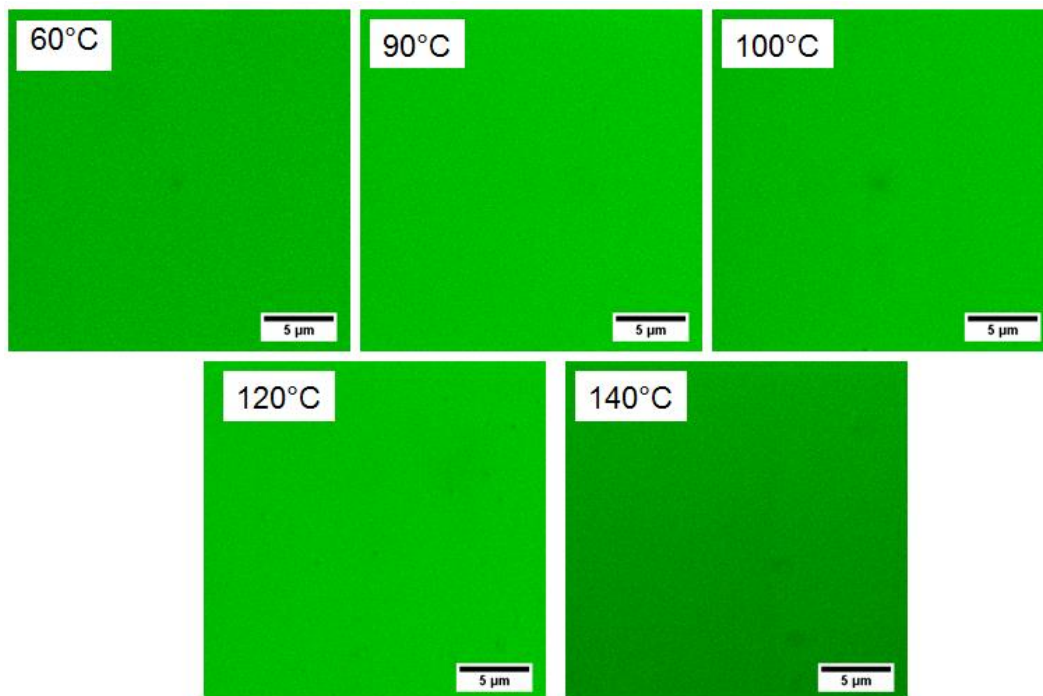


Figure 3.4. Confocal fluorescence microscopic images showing the effect of annealing temperature on phase separation of the PS₂₁/PMPS₁₆ blend. All specimens were annealed for 24 hours at temperatures indicated in the left upper corners and measured at ambient temperature.

3.4. Kinetics of phase separation

More informative of the domain formation and growth is the *in situ* observation of the phase separation dynamics at elevated temperatures. In this experiment the PS₁₁₆/PMPS₁₆ blend is brought to 120°C and immediately started to be imaged. Some representative images at selected times are shown in Figure 3.5.

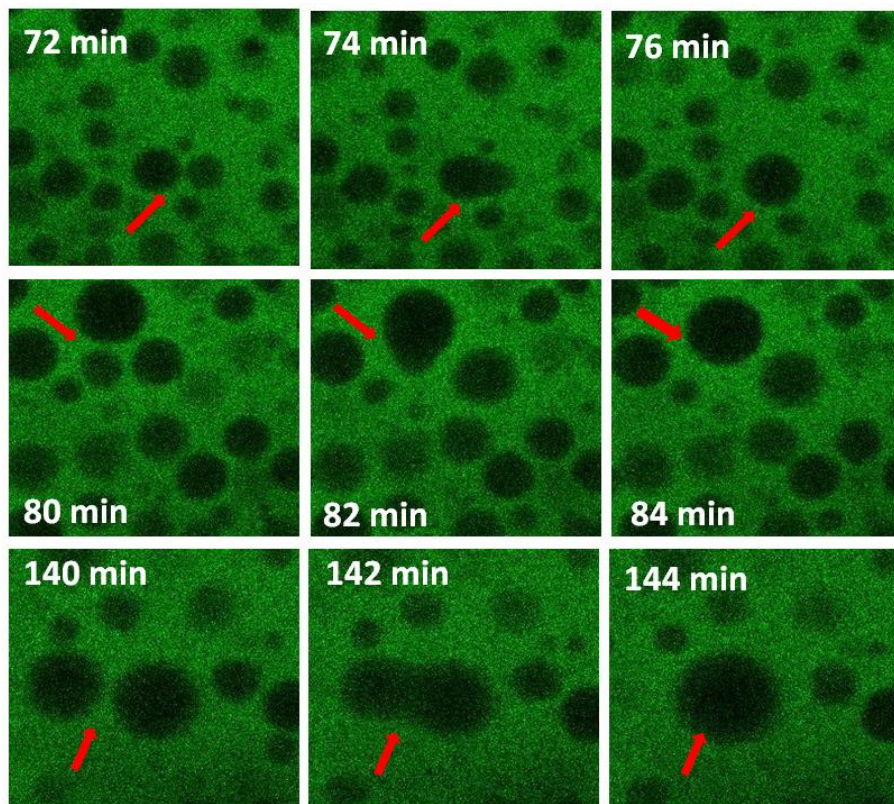


Figure 3.5. Droplet approach (left), coalescence (middle) and subsequent growth (right) obtained *in situ* for the PS₁₁₆/PMPS₁₆ blend. Images were recorded at 120°C at different times as indicated. The arrows point towards the “interesting” droplets.

First, it appears that the PMPS-rich phase is nucleated in rows (left corner at $t=42$ min). Subsequently, when the dark grains reach an appreciable size they coalesce.

During this process the grains are deformed from their spherical shape due to the acting elastic forces (Figure 3.5, middle). Eventually, the larger grains absorb the smaller ones. At intermediate times not shown in Figure 3.5 some already grown grains disappear completely. This reflects the coalescence of these grains with even larger grains located above or below the focal plane.

The late stages of grain growth from a supersaturated solid solution have been investigated theoretically by Lifshitz and Slyozov. [97] Initially, concentration fluctuations give rise to nuclei of the new phase whereas at a later stage the growth of larger grains - with dimensions above a critical dimension R_c - proceeds by the incorporation of smaller ones. The theory predicts the details of the grain growth from the distribution function of grain dimensions. The growth rate is predicted to follow: [97]

$$\dot{R} = \frac{2\gamma}{\zeta R} \left(\frac{1}{R_c} - \frac{1}{R} \right)$$

Here, γ is the surface tension and ζ is the friction coefficient. At late stages in particular, the critical dimension, mean grain dimension, and number of grains are predicted to scale as $R_c \sim t^{1/3}$, $\langle R \rangle \sim t^{1/3}$ and $n \sim t^{-1}$, respectively. Subsequently, Onuki, [97] studied the influence of viscoelastic effects. In this case the surrounding semidilute region is deformed in the radial direction giving rise to a large viscoelastic stress. In the presence of such viscoelastic effects one needs to define two length scales: the domain size (R) and the viscoelastic length, ξ . They give rise to a modified Lifshitz-Slyozov equation:

$$\dot{R} = \frac{2\gamma}{\zeta R} \left(\frac{1}{R_c} - \frac{1}{R} \right) / \left(1 + 3 \frac{\xi^2}{R^2} \right)$$

where $\zeta = (4\eta/3\dot{\zeta})^{1/2}$ and η the zero shear viscosity. In polymer blends, ζ cannot exceed the tube length, hence $R \gg \zeta$ and eq. 1 is valid for large droplets.

Herein using the results of the *in situ* monitoring we plot the mean grain dimension ($\langle 2R \rangle$) and number of grains (n) for the PS₁₁₆/PMPS₁₆ blend during annealing at 120°C in Figure 3.6. For the shorter times, both $n(t)$ and $\langle R \rangle(t)$ deviate from the predictions for late stage SD. This suggests that at $t < 10^3$ s, the blend is in the *elastic* regime where the domain shape is determined by a balance between the elastic forces and the interfacial tension. [98] Within this regime the composition of each phase changes with time by the diffusion of PS from the PMPS-rich phase to the PS-rich phase. Furthermore the area fraction of the less viscoelastic phase (PMPS-rich) is about 0.3, i.e. much below the PMPS blend composition. The low fraction is in agreement with the results from the earlier DS investigation that identified a substantial PMPS fraction within the PS-rich phase. [81]

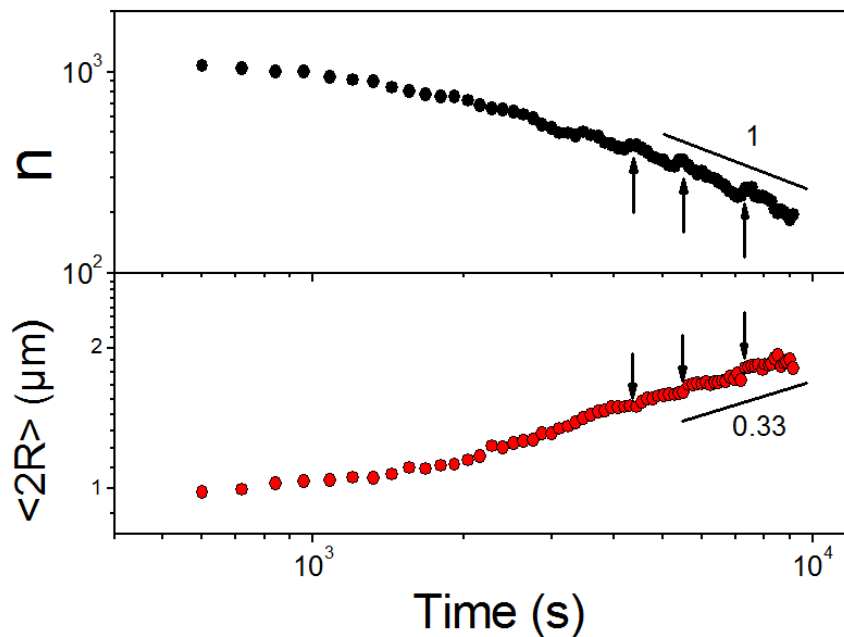


Figure 3.6. Evolution of the number of grains (top) and mean grain dimensions (bottom) for the PS₁₁₆/PMPS₁₆ blend at 120°C. The vertical arrows indicate the times where grains move out of the focal plane and coalesce with larger grains. This affects both their number and average grain dimension. Lines with slopes of 1 (top) and 0.33 (bottom) are shown.

3.5. Purity of domains

The LSCM images shown above do not have enough contrast to account for small amounts of fluorescently labeled PS that may be present within the PMPS phase. Below we will show that the technique of FCS when coupled with LSCM can provide additional information on the purity of phases in individual domains with sub-micrometer spatial resolution.

As discussed in details in Chapter 2, FCS is based on monitoring and recording the fluorescent intensity fluctuations caused by the diffusion of single fluorescent species through the focus of a confocal microscope. Autocorrelation analysis of these fluctuations yields the diffusion coefficient of the species. To enable FCS, small amount of the fluorescent dye TDI was introduced as tracers in the PS₁₁₆/PMPS₁₆ blend. It should be stressed that the absorption maximum of TDI is around 630 nm i.e. far away from that of fluorescein (~480 nm) used for labeling the PS phase. Thus, the two dyes can be excited individually by different lasers and their fluorescence can be detected also individually. The procedure was as follows: prior to the FCS measurement, LSCM images were recorded using excitation at 488 nm (for fluorescein labeled PS) and then the laser focus was pointed in the center of a chosen PMPS domain and the excitation wavelength changed to 633 nm (for the TDI). (Figure 3.7)

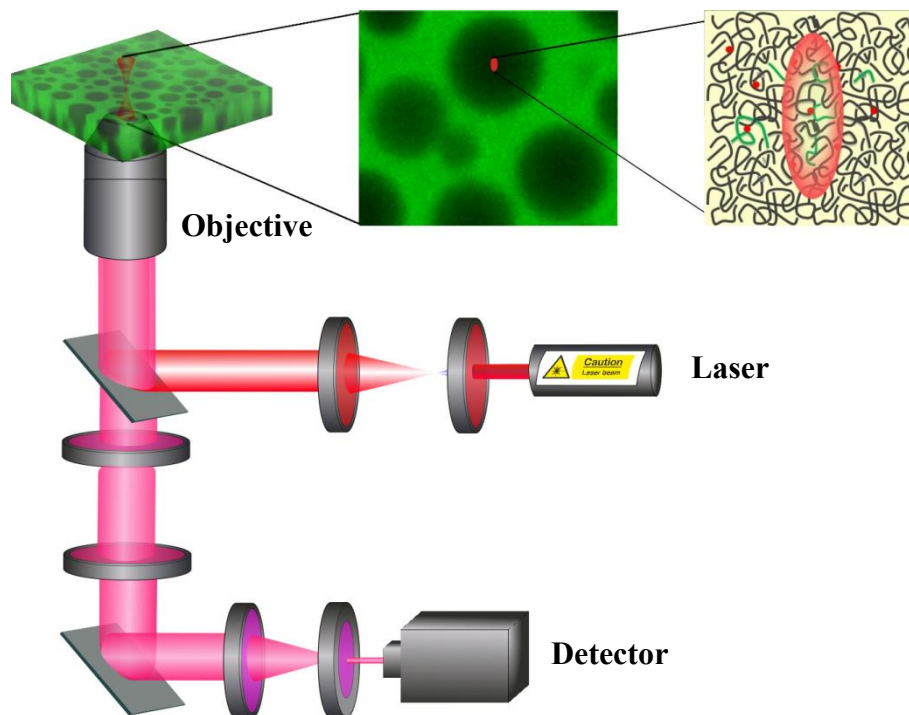


Figure 3.7. Sketch illustrating the performance of FCS measurements in PMPS domain of the phase separated polymer blend.

The time-dependent fluctuations of the fluorescent intensity caused by the diffusion of the TDI tracers through the focus were recorded and the corresponding autocorrelation curves yield the tracer diffusion time and diffusion coefficient. Subsequently, a new position was chosen within the PMPS-rich domain by moving the focus by $1\ \mu\text{m}$ away from the center and the auto-correlation curve was obtained (Figure 3.8b)

This procedure was repeated at $1\ \mu\text{m}$ increments from the center of the domain up to the domain boundaries. Measurements were performed in domains with different sizes from 3 to 20 microns.

Typical results of the FCS measurements for the PS₁₁₆/PMPS₁₆ blend first annealed at 120°C for 24 h and subsequently quenched at ambient temperature and measured after a period of ~2 h are shown in Figure 3.8a.

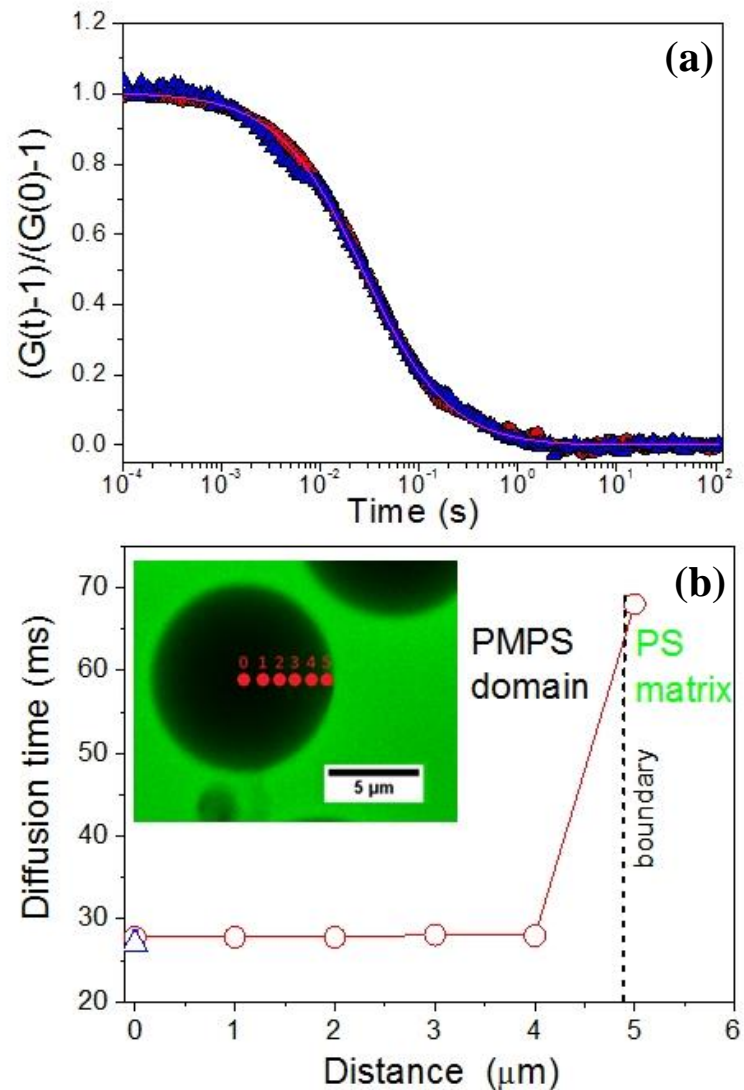


Figure 3.8. (a) Normalized autocorrelation curves of terylene dye diffusing in bulk PMPS (●) and within the PMPS domain (▲) of the PS₁₁₆/PMPS₁₆ blend. (b)

Diffusion times of terylene dye as a function of measuring position within the PMPS-rich domain of the LSCM image (○). The diffusion time of the same dye in bulk PMPS (Δ) at the same temperature is also shown for comparison. The line is a guide to the eye.

The Figure depicts normalized autocorrelation curves of TDI corresponding at position 2 of the LSCM image.

For comparison, the autocorrelation curve for the diffusion of the same dye in a PMPS homopolymer at ambient temperature is also shown. The figure further compares the diffusion times as a function of the measuring position within the PMPS grain. We can deduce that the TDI tracer is diffusing freely (according to the Fick's law) with nearly identical diffusion times in all cases.

Thus, the results shown in Figure 3.8 indicate that the large dark domains are composed nearly exclusively by PMPS chains. This finding may sound paradoxical since it is the experience with polymer blends that one of the coexisting phase contain at least some amounts of the counter component. However, a closer inspection of the PS/PMPS phase diagram (Figure 3.1) reveals that at ambient temperature the PMPS phase is exclusively composed from PMPS chains.

To explore further this point a strongly asymmetric PS₁₁₆/PMPS₁₆ blend was prepared (2/98) with the outlined procedure and imaged with LSCM. In Even at this composition phase separated PS domains were clearly observed (Figure 3.9) in accord with the phase diagram. In addition, the result is in excellent agreement with the local segmental relaxation of PMPS in the PS₄₈/PMPS₁₇ symmetric blend investigated earlier with dielectric spectroscopy. [21]

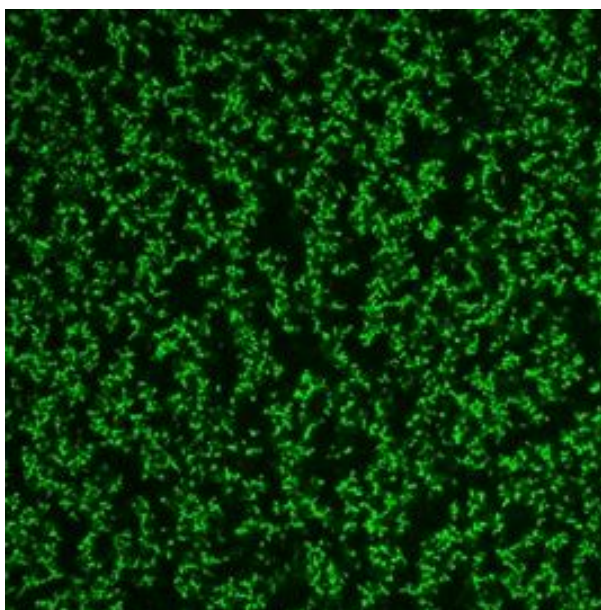


Figure 3.9. Confocal fluorescence microscopic image of an asymmetric (2/98) PS₁₁₆/PMPS₁₆ blend annealed and measured at ambient temperature revealing phase-separated domains.

These results have shown that $\phi_{\text{PMPS}}^{\text{PMPS-rich}} \sim 1.0$, i.e. a nearly pure PMPS phase. The reason for the different compositions in the two phases is that the PS glass temperature can intervene to the process of phase separation resulting in a hard component that cannot attain its equilibrium composition. On the other hand, the soft component (PMPS) can easily attain its equilibrium composition as observed experimentally.

With respect to Figure 3.8, it is only at the domain boundaries that the diffusion time (which is reversed proportional to the tracer diffusion coefficient) increases by a factor of two suggesting mixing of PMPS chains with the slower PS chains.

To test the sensitivity of FCS towards the purity of the PMPS domains the same PS₁₁₆/PMPS₁₆ blend was again annealed at 120°C for 24 h and quenched at ambient temperature but then immediately investigated by FCS as a function of time.

Under such conditions the PMPS-rich phase may contain some slower PS chains. All measurements were made at the center of the domain and the result is shown in Figure 3.10, which depicts the diffusion time of TDI in the center of the PMPS rich domain as a function of the time after quenching from 120°C to room temperature. In the beginning the dye diffuses much slower than in pure bulk PMPS, indicating the presence of remaining PS chains.

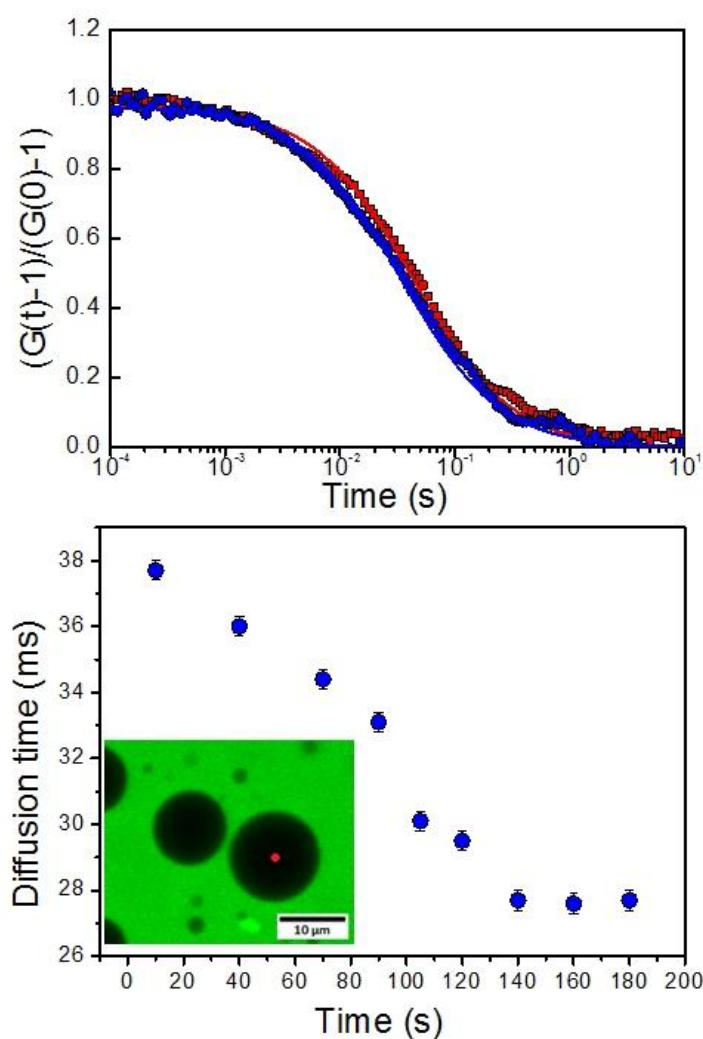


Figure 3.10. (Top) Normalized autocorrelation curves of TDI diffusing within the PMPS domain directly after quenching from 120°C to room temperature (filled circles) and in the same PMPS domain after 3 hours (filled squares) of the PS₁₁₆/PMPS₁₆ blend. Measurements were made in the center of the domain. (Bottom) Diffusion times of TDI as a function of measuring time within the center of the PMPS-rich domain of the LSCM image.

Later these chains leave the domain and the diffusion time of TDI reaches a constant value similar to that measured in pure PMPS. Thus, FCS is able to track in a unique way the late stages of the phase separation inside micron-sized domains.

3.6. Conclusion

The in situ investigation of the phase separation by LSCM was coupled with ex situ FCS measurements that provided both the dynamics of phase demixing and the purity of phases in a symmetric polymer blend. This combination demonstrated the possibility to obtain independent microscopic information on the local concentration within the phase-separated domains and further allowed estimating the interfacial width of a phase-separated blend by dynamic means. It would be of interest to explore the purity of phases for other blend compositions or in other blend systems that show bicontinuous phases instead.

CHAPTER 4

Dynamics in glassy solutions of star shaped polymers

4.1. Introduction and motivation

In the past twenty years soft matter has become a field of growing interest. [99] First reason is that soft matter is in our everyday life (blood, clay, plastics, DNA, proteins, etc.). Another one is soft matter has by now reached even technological relevance, for example in biotechnological or pharmaceutical applications. [100] Among the systems comprised in soft matter (liquids, gels, foams, polymers, granular materials, etc.), colloidal suspensions represent a large and prominent field.

Since years it's known that by increasing the volume fraction, colloidal suspensions reach a frozen state. In a hard sphere suspensions, when the volume fraction exceeds the value of 0.58 any of the given particles is surrounded with up to 12 neighboring particles and this restrict macroscopic motion, and thus the whole suspension undergoes transition to a dynamically arrested state, which is glass. [101] The glass formation is discussed in the context of caging (Figure 4.1), [102] particles remain trapped in cages and there is only in-cage motion present, which constitute the β -relaxation process. After some time particle escapes from the cage, which leads to terminal relaxation; this process is called α -relaxation. In order to describe glassy dynamics in hard spheres, especially in the linear response regime, various versions of the mode-coupling theory (MCT) were provided. [103, 104]

Another attractive system is soft colloidal suspensions; such are for example multiarm star shaped polymers, which consist of f chains chemically anchored on a common center. By variation of functionality f one can control the softness of the colloids. (Figure 4.2 image taken from [105]) The glass formation of soft star polymers can also be formulated in context of caging. However in comparison to hard spheres there interaction is softer, and being deformable, stars can interpenetrate at higher concentrations. The polymeric nature of stars adds some interesting features. Due to their partial interpenetration, the outer blobs of the neighboring caged particles form effective entanglements, and therefore α -relaxation proceeds through both factors: disengagement of the stars from neighbors and cage opening like in case of hard sphere colloidal glasses.

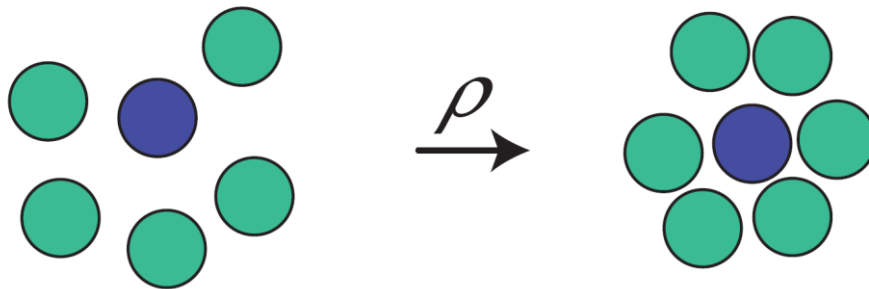


Figure 4.1. Cartoon representing caging for hard spheres.

Although these materials macroscopically behave like a glass, even at relatively low polymer concentration, at nanoscopic level the mobility is still present. [105, 106]

The aim of this project was to investigate the dynamics in these soft colloidal systems. By probing the tracer diffusion at microscopic level using FCS we can study, whether tracer and solvent molecules mobility in present system is affected by

this macroscopical “glass transition”. Additional information how the tracer dynamics can be affected by the glass transition is given in this paper. [24]

4.2. Materials and sample.

In order to study the dynamic in soft colloidal systems we used the specific star shaped polymers provided by the group of Dimitris Vlassopoulos. [105] They consist of a hard dendritic core and a soft polybutadiene outer shell. Each carbosilane dendritic core comprises 128 Si–Cl functional groups, which were first coupled to 1,2-poly(butadienyl)lithium chains with number and weight-average molar masses $M_n = 1.20 \text{ kg mol}^{-1}$ and $M_w = 1.32 \text{ kg mol}^{-1}$, respectively. The hydrodynamic radius of the colloidal stars in very dilute solutions was measured by DLS: $R_h = 40 \text{ nm}$ at $T = 20 \text{ }^\circ\text{C}$. The corresponding overlap concentration was calculated and found to be $C_h^* = 57 \text{ mg ml}^{-1}$. The detailed information of the syntheses of these colloidal stars can be found in following paper. [105]

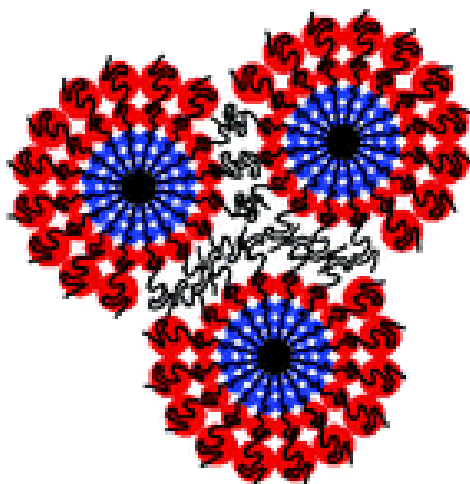


Figure 4.2. Cartoon illustration of interpenetrating stars in solution.

Rheological experiments were done on the solutions of these particles with a range of concentrations C spanning 0 to 199 mg ml⁻¹ were prepared by adding these colloidal stars to squalene [107] Figure 4.3, a good solvent for polybutadiene.

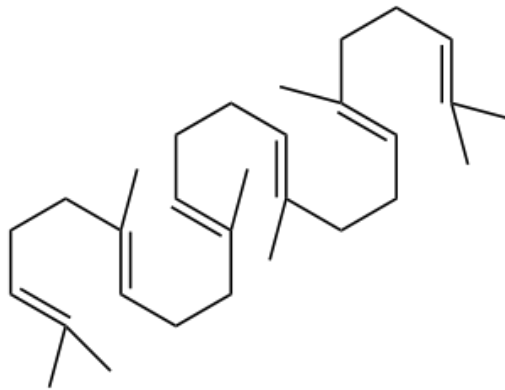


Figure 4.3. Chemical structure of the Squalene

Squalene is a natural 30-carbon organic compound originally obtained for commercial purposes primarily from shark liver oil.

In Table 4.1 a data from the experimental paper is provided. [105]

Symbol ^b	C /mg ml ⁻¹	η_0 [Pas]	σ_y [Pa]	G_0 [kPa]	Rheological state
□	199	not reached	310	5.7	Glass
○	147	not reached	140	3.2	Glass
△	131	4.4×10^6	88	2.4	Glass
▽	121	5.4×10^4	58	1.5	Glass
◇	109	1.8×10^3	27	0.59	Glass
◁	98	1.1×10^2	—	—	Suspension
▷	80	3.6×10^0	—	—	Suspension
◊	59	3.0×10^{-1}	—	—	Suspension
☆	30	4.5×10^{-2}	—	—	Suspension
+	0	1.5×10^{-2}	—	—	Solvent

Table 4.1. Star solutions studied: plotting symbols, concentrations, viscoelastic properties (zero-shear viscosity, yield stress and plateau modulus determined from oscillatory measurements) and rheological state

In order to prepare the concentrated solutions for FCS measurements, tetrahydrofuran (THF) was added in excess as a co-solvent in order to promote dispersion and mixing of the stars. Under continuous mixing the THF was evaporated away with vacuum applied as a finishing step to assist in the full removal of the co-solvent. In addition TDI was added with concentration $10^{-9} \text{ g mol}^{-1}$

4.3. Tracer diffusion in star shaped polymer solutions

Star shaped polymer solutions in squalene were prepared with concentrations ranging from 10-50 weight %. Solution was putted on the microscope glass slide, was fixed in attofluor chamber (Figure 4.4), and mounted on the microscope.

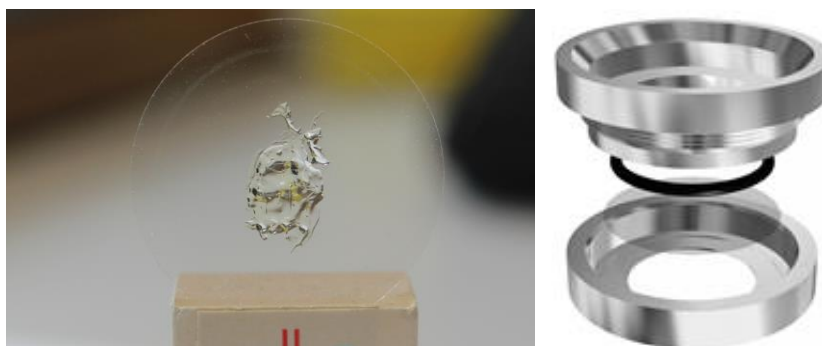


Figure 4.4. Cartoon illustrating how the sample was prepared for FCS measurements

The FCS measurement was performed in the middle of the “glassy” polymer above the glass surface. The example of autocorrelation curves of TDI dye in the “glassy” polymers at different concentration is given in Figure 4.5.

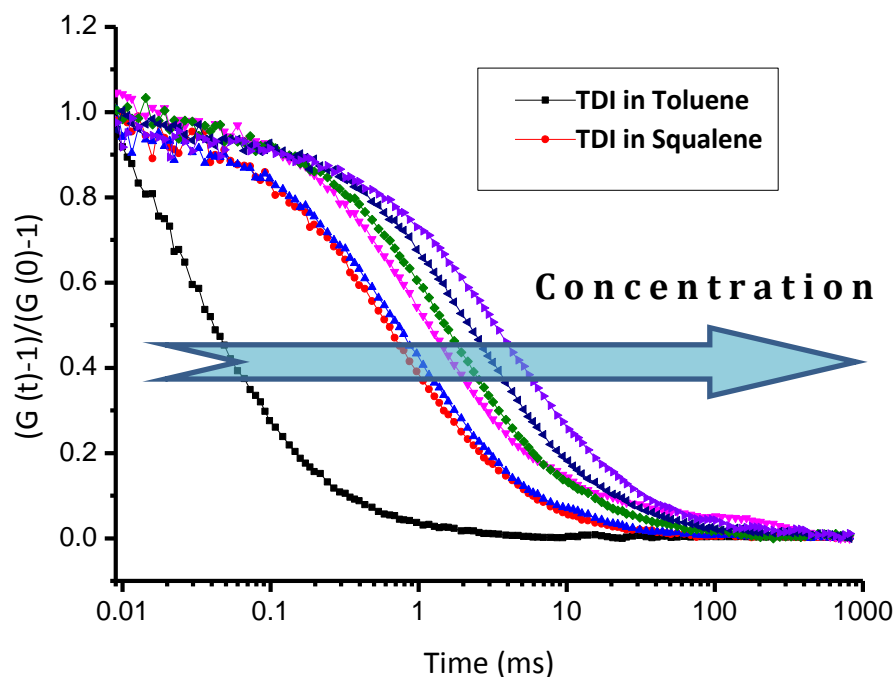


Figure 4.5. Normalized autocorrelation functions obtained for TDI diffusing in bulk toluene, bulk squalene and in “glassy” polymer solutions, by increasing the weight % of the polymer by 10% each step.

First TDI was measured in pure squalene, and after that the concentration of the polymer was set to 10 weight%, next step the concentration of the polymer was further increased till 20% and so by step of 10% till 50%. Curve of TDI diffusing in bulk toluene is given for a comparison. To be sure in the reproducibility of the results, measurements were performed several times at different position through the thickness of the glassy polymer film. All the autocorrelation curves were fitted with the single component diffusion model.

From Table 4.1 we can see that the that the rheological state of the polymer solution changes from “suspension” to glass when we go from concentration 98 g ml^{-1} to 109 g ml^{-1} . If we recalculate the concentration, in our case this jump should appear at

concentration about 30%. However as can be seen from the Figure 4.6, the TDI diffusion time increases monotonically with the increase of the star polymer concentration over the entire studied range and nothing peculiar happens and the concentration of “glass transition”. Thus, we see that the small molecule still “freely” diffuses in the polymer solution, even though macroscopically the solution is in glassy state.

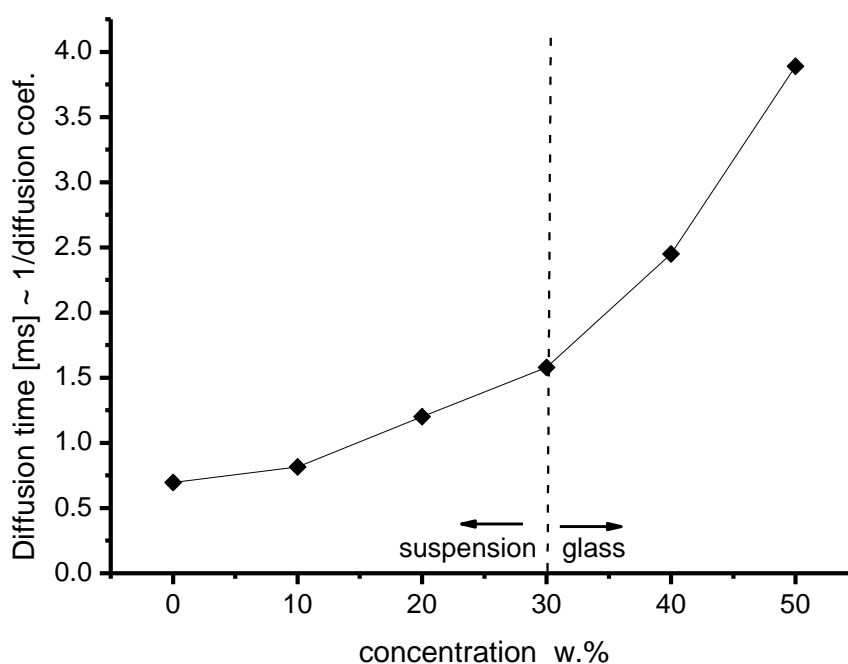


Figure 4.6. Striking difference between macroscopic and microscopic properties: the macroviscosity increase strongly with concentration and above ~30% glassy behavior and in contrast the small tracer diffusion decrease only slightly and continuously with concentration

This can be explained by the formation of the channels between the polymeric “stars”, which due to their size cannot come close to each other. There is some space

left in between the “stars”, which is more than enough for the small molecule like TDI to diffuse without restriction.

In Figure 4.7 we have plotted the normalized TDI diffusion coefficient (on the value measured in pure squalene) vs. the star shape polymer concentration in order to compare our results with existing data for the diffusion of various small tracers in solutions of linear polymers that have been shown to fall on a single “master curve”. The plotted master curve presents reported diffusion coefficients for polymer systems obtained by measuring by different experimental techniques [108] Meerwall et al. [109] studied the diffusion of hexafluorobenzene in PS (10k to 1000k)/THF solutions by pulsed field gradient spin-echo NMR. Chekal and Torkelson [110] reported behavior of a styrene monomer diffusing in polystyrene solutions down to a matrix PS molecular weight M_w of 1300 g/mol. More recently diffusion of a small PMI dye in polymer solution studied by FCS was reported. [23] All the presented data from the literature indicate that the polymeric nature of the matrix expressed by its molecular weight or that is the same by its crossover concentration does not affect the small probe behavior. Instead it is only the crowding effect of the environment molecules that reduces the diffusion rate of the small probes in such solution.

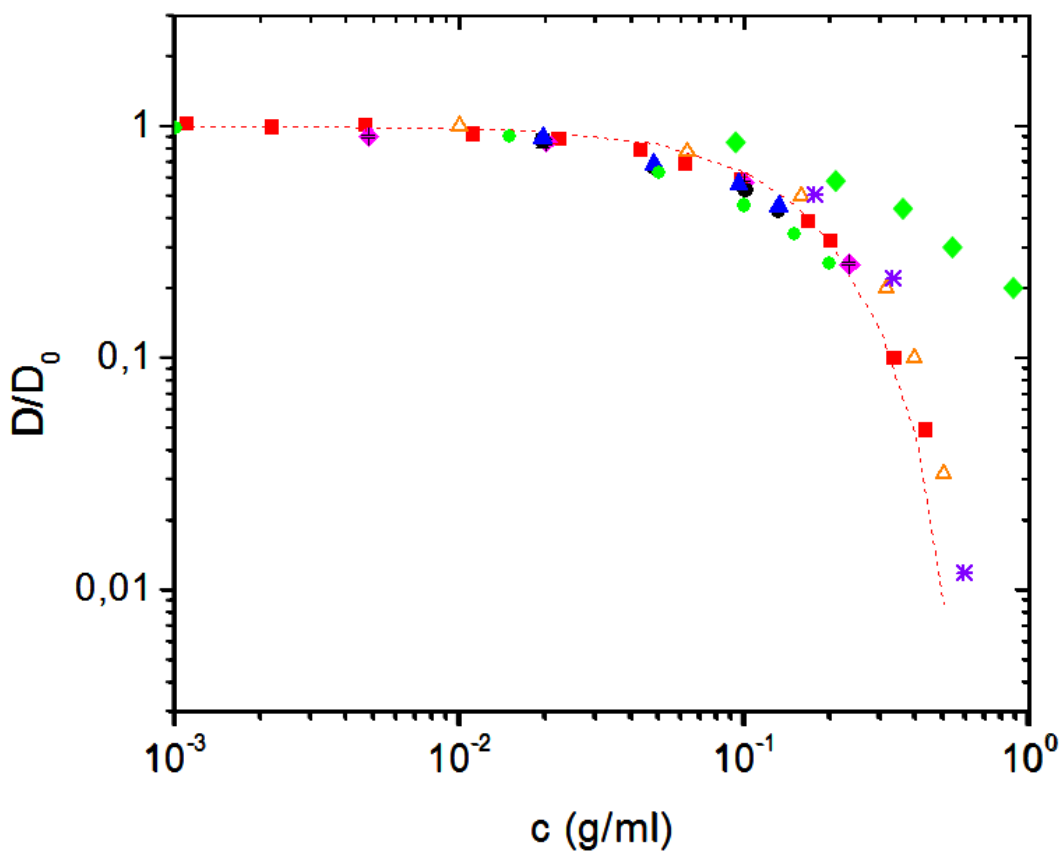


Figure 4.7. Normalized diffusion coefficients of various small tracers. Green rhombs represent the data for the TDI in star polymer/squalene solutions.

From my studies which, correspond to green rhombs on the plot Figure 4.7 we can see that tracer slowdown is even smaller in the present system of star shaped polymers as compared to the linear polymer solutions. This can be considered as a further evidence that the channel can form between the polymeric stars and facilitate the diffusion.

In order to address the size dependent diffusion in “glassy” polymer solution, I decided to study the diffusion of the bigger fluorescent tracers. Qdots which have size in radius of about 5nm and the excitation maximum 633nm were used. Before

putting the Qdot in “glassy” polymer solution, the reference measurements were done. First I checked Qdot diffusion in toluene and after Qdot diffusion in squalene. As one can see from Figure 4.8 Qdot diffuses freely in toluene, and obtained autocorrelation curve can be fitted with the one component diffusion model. However, in case of squalene obtained autocorrelation curve cannot be fitted with the single component model, and two component diffusion model is needed. The reason for this can be poor solubility of Qdot in squalene, and formation of the bigger aggregates. Thus, I did not performed further studies in star shaped polymer / squalene solutions.

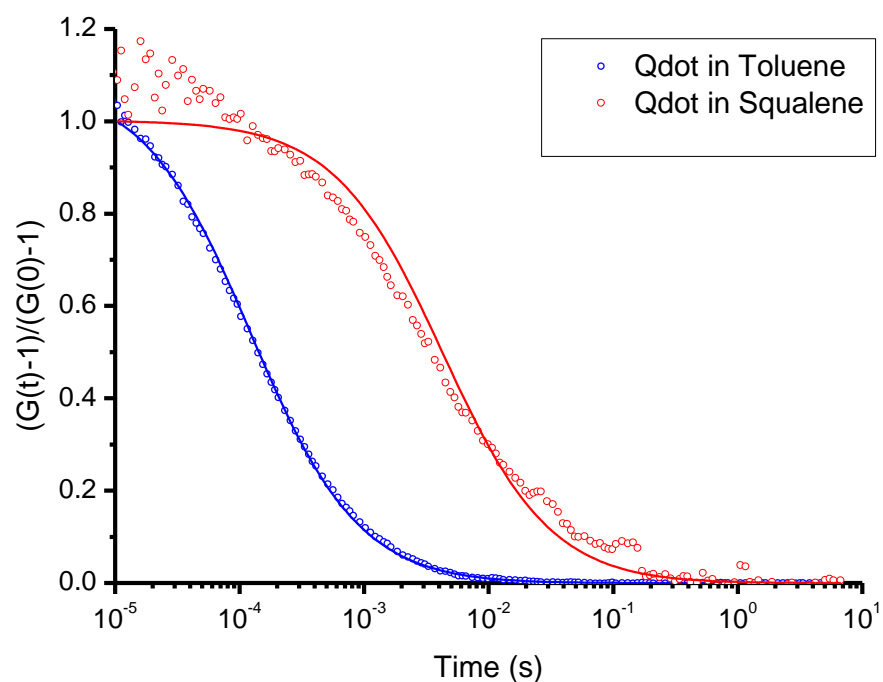


Figure 4.8. Normalized autocorrelation functions obtained for Qdot diffusing in bulk toluene (blue curve), and Qdot diffusion in squalene (red curve)

4.4. Conclusion

Diffusion of the small fluorescent dye TDI was studied using Fluorescence Correlation Spectroscopy in star shaped polymer solutions, at different dilutions. FCS measurements showed that even though the polymer solution above the concentration of 30 weight % macroscopically has properties of “glass” the microscopically the tracer mobility is still present and not affected by the transition to the glassy state. The small dye can “freely” diffuse in a “glassy” polymer solution through the microscopic channels that form between the dendritic stars. In order to address the size dependent diffusion, a bigger fluorescent dye namely Qdot with the radius of 5.5 nm was also studied in the system, however due to the aggregate formation in the solvent squalene could not give reliable results. Further studies with other tracers and with fluorescently labeled stars are currently underway.

CHAPTER 5

Temperature controlled diffusion in PNIPAM modified Silica Inverse Opals

5.1. Introduction and motivation

Understanding and controlling the diffusion of small molecules, macromolecules and nanoparticles in complex, nanostructured environments is of paramount fundamental and technological importance. A number of theories and models have been introduced to describe the diffusion of small species in polymer systems, in intercellular matrices or in solid periodic nano-porous structures.

From applications point of view, the possibility for on demand control of the diffusion of small penetrants in nanoporous structures is even more important. Indeed, such possibility gives various opportunities as to e.g. control the drug release rate or to select the relevant sizes in a separation process. Traditionally, control over the penetrant diffusion is achieved by changing the size and/or density of the nanopores. However, in a solid nanoporous structure, such as, an anodized aluminum membrane, a porous glass or a silica inverse opal, the pore size is determined during the fabrication process and typically cannot be changed e.g. by applying an external stimulus. This is unfortunate, because on the other hand the solid nanoporous structures offer the mechanical strength and stability that is required for most applications. Alternatively, in some polymer based nanoporous systems such as e.g. hydrogels, the pore size and thus the penetrant diffusivity can be controlled by tuning the temperature or the pH value. Hydrogels, however, lack mechanical stability that often makes their application problematic.

In this project, I will describe a new system combining the mechanical stability of a solid nanoporous structure with the possibility for fine tuning offered by a thermo responsive polymer. As a solid support I used a silica inverse opal (iOpal), which is a highly order porous structure, consisting of regular arrangements of spherical voids surrounded by solid silica walls with interconnecting circular pores.[111-114] Due to their well-defined nanoporous structure iOpals have been often used as model systems to study the diffusion of small molecules [24], nanoparticles or DNA. [115] Here, I modified the iOpal interior surface with grafted Poly(N-isopropylacrylamide) (PNIPAM) brushes. The PNIPAM is one of the most popular thermo responsive polymers and exhibits a lower critical solution temperature (LCST) of around 32°C [116] i.e. close to the humans body temperature. In aqueous solutions, below the LCST the PNIPAM chains are hydrated and adopt an extended coil conformation, while above the LCST they are dehydrated and collapse to a globular conformation. Correspondingly, the PNIPAM brushes grafted to the iOpal interior surface will swell under the LCST decreasing the overall porosity of the system and shrink above the LCST increasing the porosity (Figure 1). This offers the possibility for a temperature control over the diffusivity of small penetrants inside the iOpal.

PNIPAM, grafted on porous silica nanoparticles [117] or porous silicon films[118] was used previously for temperature controlled entrapping and release of model drug molecules. Here, I go a step further and focus on direct monitoring of the penetrants mobility inside the PNIPAM modified iOpals. For this purpose I used fluorescence correlation spectroscopy (FCS) (Detailed description of FCS Chapter 1) as it has very small probing volume ($< 1 \mu\text{m}^3$) that can be easily positioned on various places in the studied nanoporous structure and thus provide local information on the penetrant mobility.

5.2. Materials and sample preparation

5.2.1. Silica Inverse Opals

5.2.1.1. Preparation via Vertical Deposition method

Initially Silica inverse opals (iOpals) were fabricated using Vertical Deposition (VD) method (Detailed description in Chapter 1) Monodisperse PS colloids of 100-1000 nm and 7nm silica nanoparticles were co-deposited from aqueous suspension on round microscope glass slides (Menzel, Germany) with diameter and thickness of 25 mm and 0.17 mm respectively. Procedure is illustrated in Figure 5.1.

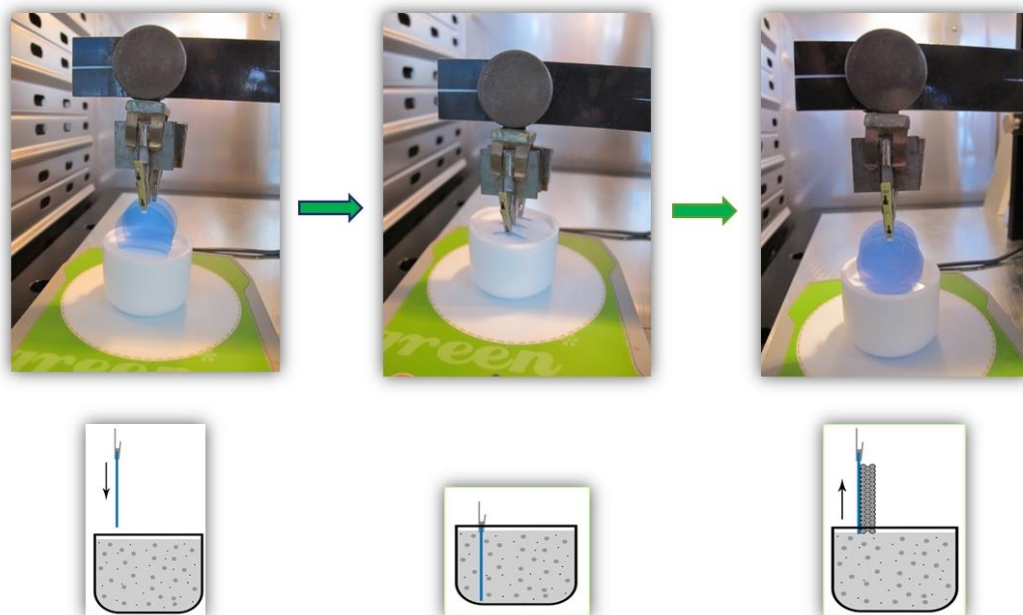


Figure 5.1. Preparation of colloidal crystal in humidity chamber via VD deposition method. White Teflon vessel is filled with the mixture of Polystyrene and SiO₂ nanoparticles. The microscope cover glasses are covered from one side with the blue polyethylene films to avoid the crystal formation on this side.

Prior deposition, glass slides were cleaned by a 2% Hellmanex solution (Hellma, Germany) and hydrophilized by a plasma treatment. In addition in order to have a formation of the opal only on the one side of the glass, the other side was covered with the commercially available polyethylene film.

VD was performed in a temperature range 20-25°C and humidity 30-80%, in a special humidity chamber with the lifting speed from 200 nm/s to 800 nm/s. Concentration range of PS colloids was 0.5 – 4 wt%, whereas SiO₂ particle concentration was kept constant 0.3 wt%.

Inversed SiO₂ opals were obtained after removal of the PS spheres by calcination at 500 °C for 5 h. (Figure 5.2.)

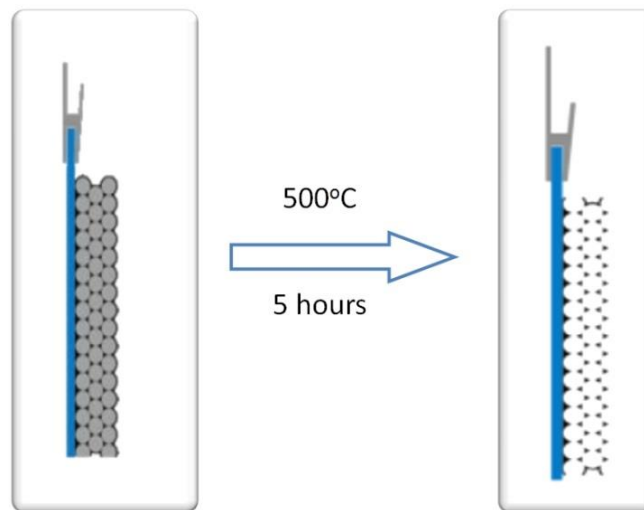


Figure 5.2. Removing polystyrene template via calcination at 500°C, after 5 hours the well order structure of SiO₂ is left.

The quality and size of the dry inverse opals were characterized by scanning electron microscope (SEM) Figure 5.3. From the SEM images we can see, that opals have voids with the size comparable to the PS particle size from which they were fabricated. And these voids are connected to each other with the holes.

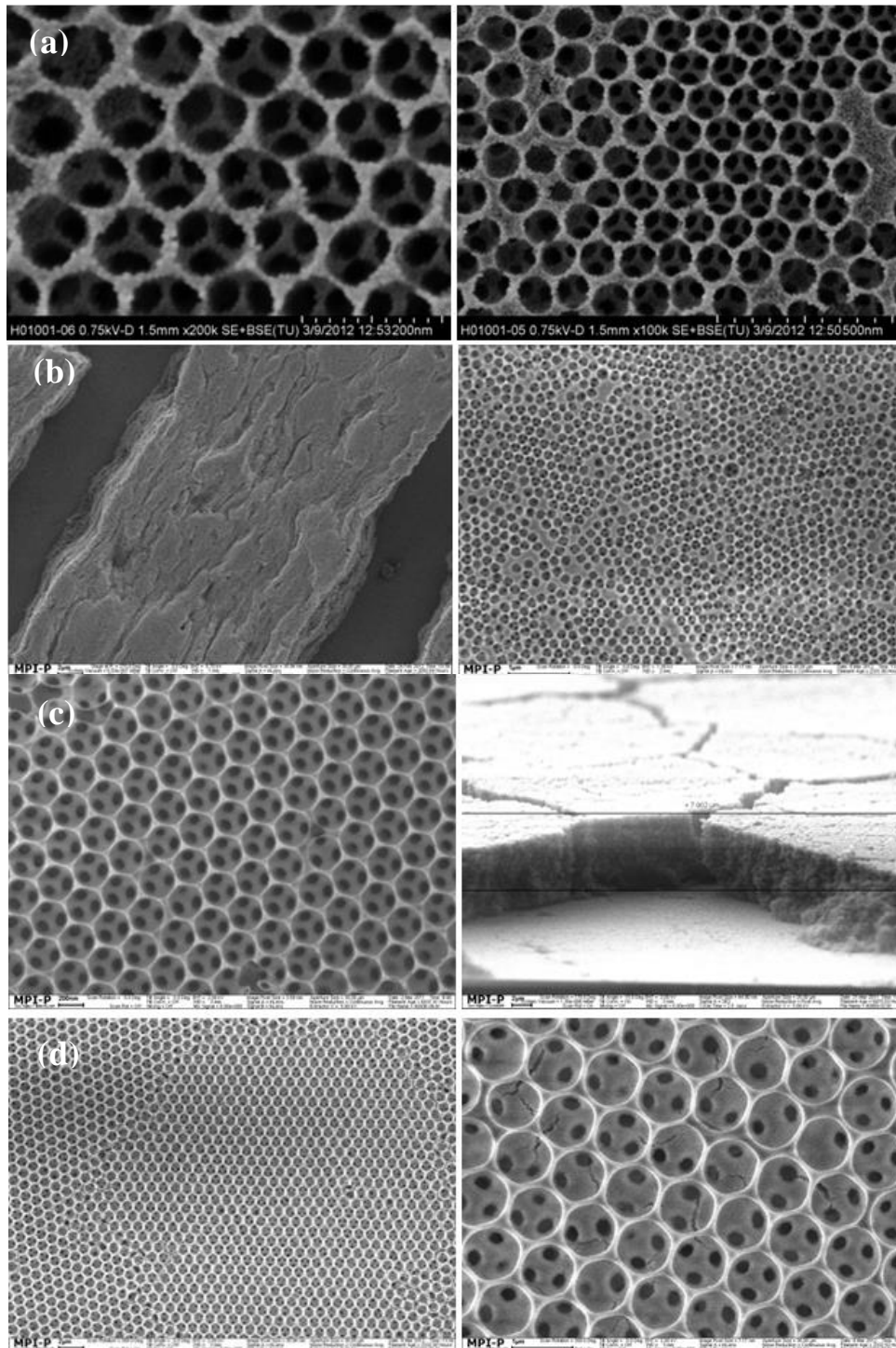


Figure 5.3. Scanning electron microscopy images of inverse opals made from (a) 100nm, (b) 200 nm, (c) 300 nm and (d) 1000 nm polystyrene particles.

5.2.1.2. Modification via ATRP

Silica Inverse Opals with a void diameter 300 nm (Figure 5.4c) were modified with thermoresponsive polymer brushes via Atom transfer radical polymerization (ATRP) method (Detailed description in Chapter 1). Gel Permeation Chromatography (GPC) method was used to determine molecular weight of the polymer obtained from bulk polymerization.

5.2.1.2.1 Materials

N-Isopropylacrylamide (NIPAM), CuBr, Ethyl 2-bromoisobutyrate were purchased from Aldrich. 1,1,4,7,7-Pentamethyldiethylenetriamine (PMDETA) was purchased from Acros. The starter 3-(2-bromoisobutyryl)propyl)dimethyl chlorosilane was synthesized following the procedure described in the literature. [119] NIPAM monomer was recrystallized from hexane. CuBr was purified by boiling in mixture of 1:1 (by volume) Millipore water/ acid acetic and subsequently filtered off. The precipitate was rinsed with water, ethanol, and finally with diethyl ether and dried in a vacuum oven for 24 h. (2-EiBBr) (Aldrich, 98%) was used without further cleaning. Toluene was distilled from sodium under Argon atmosphere. Triethylamine was distilled from CaH₂ and stored under Argon atmosphere. All aqueous solutions were prepared with ultrapure water purified with a Milli-Q UV-Plus water purification system (Millipore, Bedford, MA). The water had a resistivity of >18MΩcm⁻¹.

5.2.1.2.2 Initiator Immobilization

In order to prepare the silicon surface for the starter immobilization and to assure controlled hydration state of the silicon oxide layer on top, a base cleaning was performed. Silica inverse opal was immersed in a mixture of NH₃ (4 mL, 25%),

H₂O₂ (4 mL, 35%) and Millipore water (50 mL) at 80 to 85 °C , for 20 min. Afterwards, the silicon surface was rinsed with copious amounts of Millipore water and dried with a N₂ flow.

The freshly cleaned silica inverse opal was immersed in a solution of dry toluene (50 mL), triethylamine (400 μL, c = 50 mmolL⁻¹) and 3-((2-bromoisobutyryl)propyl)-dimethylchlorosilane (200 μL, c = 25mmolL⁻¹). The solution was stirred for ~20 h. The sketch initiator immobilization is given in Figure 4.5. Then, the silicon objects were placed in a soxhlet apparatus and extracted with dichloromethane for 1 h dried in a nitrogen stream and used for graft polymerization.

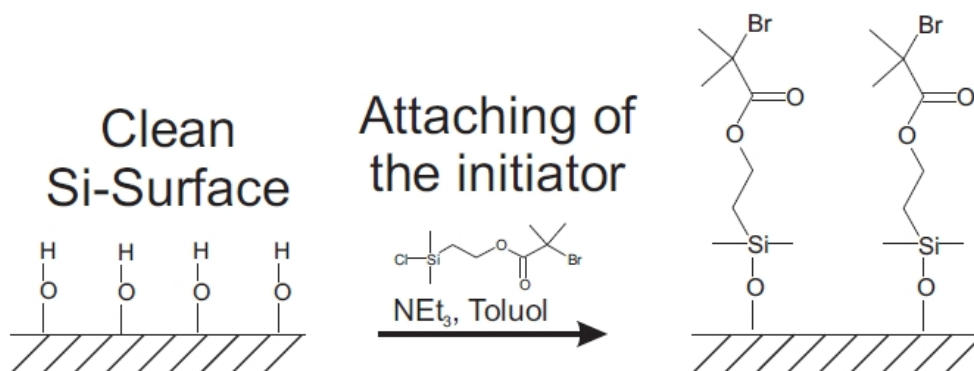


Figure 5.5. Initiator Immobilization on Silica inverse

5.2.1.2.3 Surface-Initiated Polymerizations

The surface-functionalized silicon substrate was placed in the tube and the reaction solution was prepared in DMF/H₂O (1:1, V = 28 mL) containing the monomer NIPAM (m = 2.72 g), the ATRP catalyst CuBr (m = 13.7 mg), the ligand PMDETA (V = 27,9 μL) and sacrificial initiator 2-EiBBr. The polymerization mixture was carefully degassed through several freeze-thaw cycles to remove dissolved oxygen and the polymerization was carried out at RT. After 4 h reaction

time the silica inverse opal was removed from the polymerization mixture rinsed with dichloromethane and dried.

Subsequently, they were placed in a Soxhlet apparatus, continuously extracted with toluene for 18 h, and dried. The polymer generated in solution with the initiator added sacrificially was recovered by precipitating the reaction mixture into methanol, filtering and drying in vacuum. For gel-permeation chromatography (GPC) analysis (Figure 4.6) solutions of the polymers were briefly filtered over alumina to remove residual copper complex.

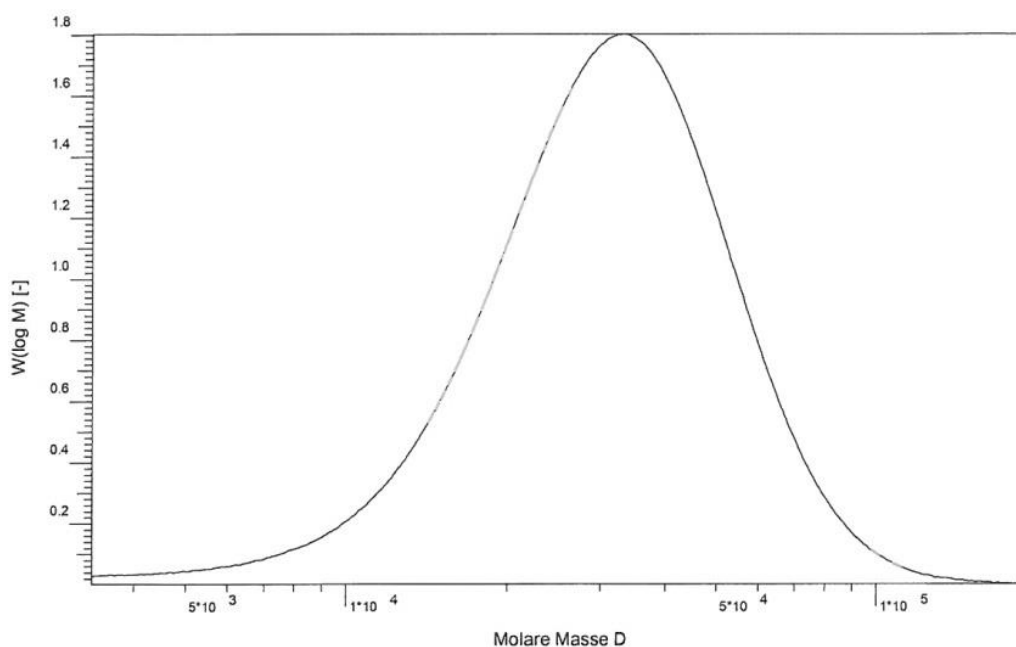


Figure 5.6. Gel-permeation chromatography of the polymer generated in the solution.

From GPC analyses polymer has a molecular weight of 25K and polydispersity $D=1.37$ Modified Silica Inverse Opals were also analysed with SEM and compared to not modified one (Figure 4.7). From the images one can see the presence of the polymer layer grafted from voids of the Silica Inverse Opal modified with PNIPAM brushes.

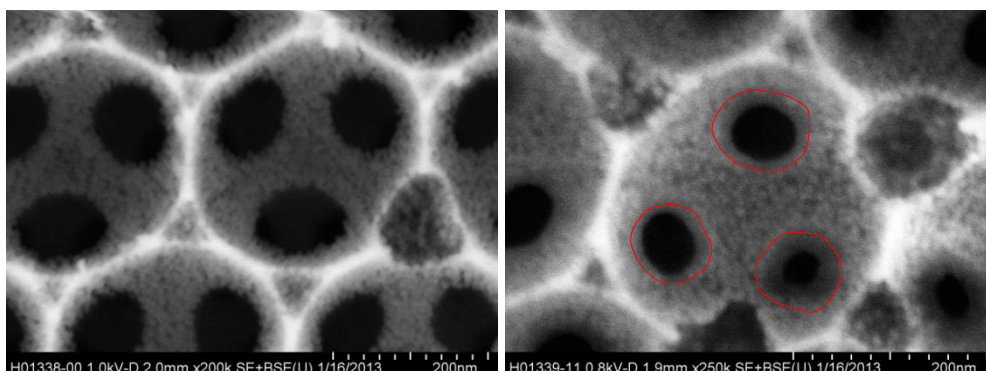


Figure 5.7. Scanning electron microscopy images of Silica inverse opal (a,b,c) and Silica inverse opal modified with PNIPAM Brushes (d).

5.3. Tracer diffusion in PNIPAM modified iOpals

We used FCS to study the effect of the grafted PNIPAM brushes on the diffusion of the small molecular dye Alexa Fluor 647 in the modified iOpals. Figure 5.8 shows a typical FCS autocorrelation curve measured in the middle of an iOpal modified with PNIPAM with $M_w=25224$. For comparison the autocorrelation curve measured in an iOpal modified only with very short PNIPAM chains ($M_w=4981$) is also shown. This sample was used as a reference instead of a completely unmodified opal in order to account for the different surface chemistry of the later that may induce adsorption of the tracers on the bare silica surface. [120] From Figure 5.8 it is obvious that the autocorrelation curve measured in the iOpal modified with long PNIPAM chains is strongly shifted to the longer lag times, reflecting significantly slower diffusion. Both curves can be nicely fitted using single component diffusion model (details Chapter 1) yielding diffusion times of $\tau_d=1200 \mu s$ and $\tau_d =140 \mu s$ in the iOpals modified with long and short PNIPAM brushes respectively. For comparison the diffusion of the same tracer in pure water is even faster (Figure 5.8) with diffusion time $\tau_d=42 \mu s$. In our experiment, the objective's immersion medium

was water with refractive index $n \approx 1.33$. For the water-filled PNIPAM modified inverse opal with silica ($n \approx 1.45$) and filling volume fraction of about 20%, the effective refractive index was $n \approx 1.36$. Due to this small refractive index mismatch, the estimated error of the diffusion coefficient in the inverse opals was less than 10%.[121-123] Thus the strong shift of the autocorrelation curves for the inverse opals toward to longer times (Figure 5.8) was caused by the confinement, as discussed and theoretically rationalized before.[123]

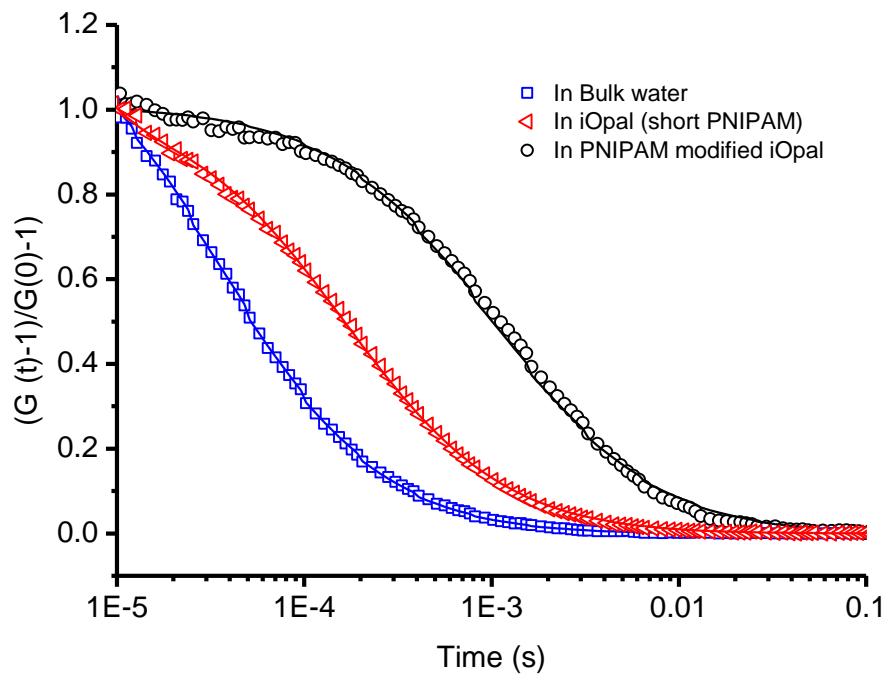


Figure 5.8. Normalized autocorrelation functions obtained for Alexa Fluor 647 diffusing in bulk water (\square), in Silica Inverse opal filled with distilled water (\square) and in PNIPAM modified Silica Inverse opal (\circ). The solid lines represent the corresponding fits.

In order to verify the reproducibility of these results, FCS measurements were performed at various lateral positions in the studied iOpals. These measurements

yielded very similar results. The situation changes qualitatively, however, when the FCS measurements were performed at different axial positions through the thickness of the iOpals. As shown in Figure 5.9, Alexa Fluor 647 molecules diffuse faster in bottom layers of the inverse opal ($\tau_d = 590 \mu\text{s}$) in comparison to upper layers of the inverse opals ($\tau_d = 590\text{-}1200 \mu\text{s}$). This indicates that the molecular weight of the grafted PNIPAM is different in different layers. Such finding is not surprising taking into account that the iOpal film is formed on a glass substrate (Figure 5.3c) and thus opened to the environment only from its upper side. During the ATRP process monomers have to diffuse through the entire iOpal film thickness in order to reach the bottom layer.

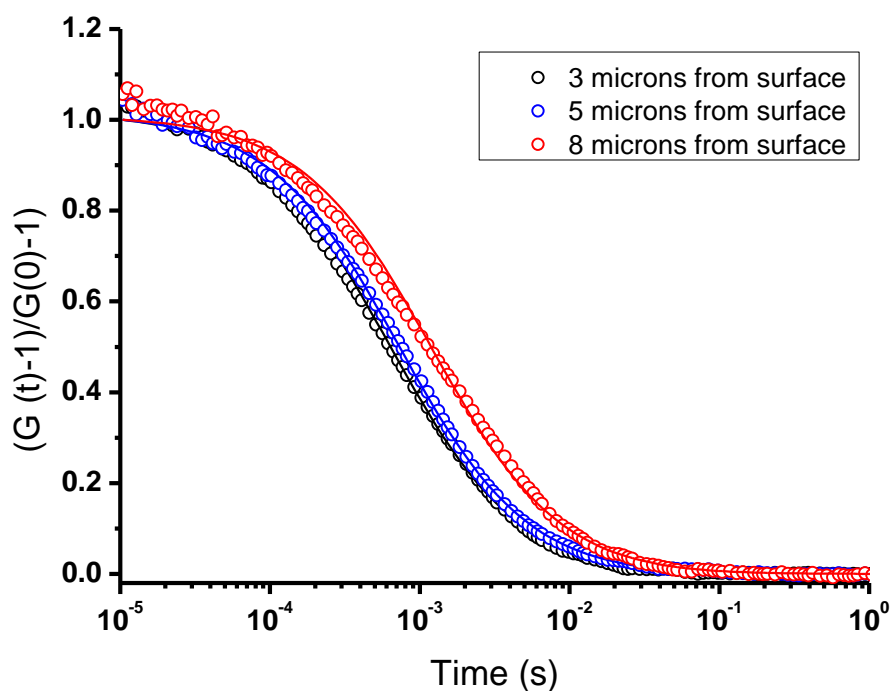


Figure 5.9. Cartoon representing the tracer diffusion in PNIPAM modified inverse opal at different distance from glass slide.

Thus the PNIPAM brushes grow faster in the upper than in the lower layers of the iOpal forming a gradient of the final brush length in the axial direction. It is important to emphasize that due to the extremely small probing volume of the FCS ($\sim 1 \mu\text{m}$ in axial direction) the small fluorescent tracer diffusion studies can nicely capture this gradient in film as thin as few micrometers only.

5.4. Temperature dependent diffusion

Now I focus on the possibility to tune the diffusivity in the PNIPAM modified iOpals by controlling the temperature and thus the PNIPAM brushes conformation and in turn the overall nano-porosity of the systems. In order to demonstrate this possibility I used FCS to study the diffusion of Alexa 647 molecules in water filled PNIPAM modified iOpal at various temperatures in the range 20°C – 35°C i.e. below and above the lower critical solution temperature of PNIPAM. For each measurement the system was kept at a constant temperature using a heating stage. The autocorrelation curves were recorded in the upper layer of the PNIPAM modified iOpal film (8 microns above the glass surface) where the length of the grafted PNIPAM brushes was maximal. Typical autocorrelation curves measured at temperatures of 20°C and 35°C are shown in Figure 5.10.

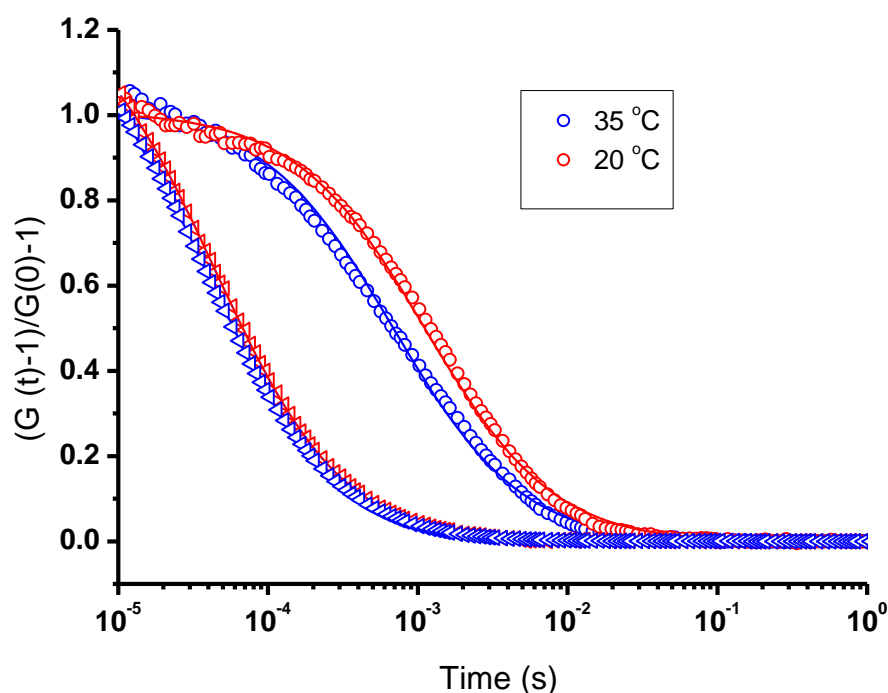


Figure 5.10. Normalized autocorrelation functions obtained for Alexa Fluor 647 diffusing in bulk water at 20 and 35 °C (\square) and in PNIPAM modified Silica Inverse opal at 20 and 35 °C (O). The solid lines represent the corresponding fits.

The curve measured at 35°C is clearly shifted to short lag times indicating faster diffusion. Both curves can be well fitted with single component diffusion model (details Chapter 1) yielding diffusion times of 693 μ s and 1237 μ s at 35°C and 20°C respectively. Table 5.1 shows the temperature dependence of the measured diffusion coefficient of Alexa 647 in the PNIPAM modified iOpals. The data are normalized to the Alexa 647 diffusion coefficient measured at the corresponding temperature in bulk water in order to account for the small temperature dependence of the water viscosity.

Temperature (°C)	Alexa 647 in bulk water	Alexa 647 in PNIPAM iOpal
20	44	1237
25	42	1170
30	40	1012
35	38	693

Table 5.1. Diffusion time versus temperature of Alexa Flour 647 in bulk water and in PNIPAM modified Silica Inverse Opal.

The data clearly demonstrate a temperature induced speed-up of the penetrant mobility in PNIPAM modified silica inverse opal caused by the stretching and collapsing of polymer brushed inside the iOpal as shown in Figure 5.11. Moreover this change in mobility is fully reversible as confirmed by repeating the measurements after several heating and cooling cycles.

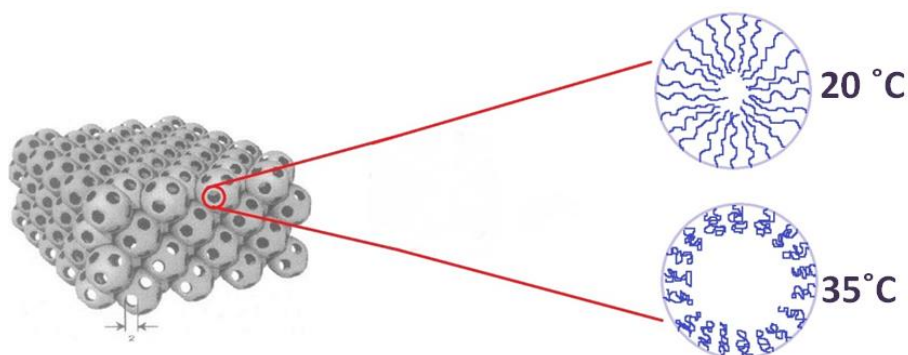


Figure 5.11. Cartoon representing the opening and closing mechanism in PNIPAM modified inverse opal at different temperatures.

5.5. Conclusion

Silica inverse Opals were modified with the termoresponsive polymer brushes via Atom transfer radical polymerization (ATRP) method and the effect of molecular crowding was investigated by Fluorescence correlation Spectroscopy. The presented results demonstrated that the dynamics in Silica Inverse Opals grafted with temperature responsive polymers brushed is becoming significantly slower. And by opening and closing interconnecting holes of the silica inverse opals, via stretching and collapsing polymer brushes the dynamics of the molecular and macromolecular tracers can be controlled.

CHAPTER 6

Summary and conclusions

Fluorescence correlation spectroscopy (FCS) is a prominent technique to investigate the diffusion of fluorescence species in various surroundings. The method is based on the measurement of the fluorescence intensity fluctuations caused by fluorescence species diffusing through a small observation volume ($V < 1\mu\text{m}^3$) of a confocal microscope. This allows FCS to address the diffusion of fluorescence species at extremely low concentration (nM), and provides a great potential to locally access systems that require high spatial resolution. Until very recently, however, FCS has been applied mainly to biological, i.e. aqueous environments.

In this thesis I used FCS to study tracer diffusion in heterogeneous systems of synthetic nature. In the first part of my thesis using the combination of the laser scanning confocal microscopy (LSCM) and fluorescence correlation spectroscopy (FCS) I studied in situ the dynamics of phase separation in the polymer blend polystyrene/poly(methyl phenyl siloxane) (PS/PMPS) at the macroscopic and microscopic length scales, respectively. LSCM was used to monitor the process of phase separation in real time providing images of droplet coalescence and growth during the intermediate and late stages. Measuring the small tracer (terrylene dye) diffusion in the PMPS phase of the phase separated blend and by comparing the diffusion of the same tracers in pure bulk PMPS, additional information on the purity of phases was obtained using FCS.

In the second part of my thesis, FCS was utilized to investigate the diffusion behavior of small fluorescent tracers in “glassy” polymer solutions. The polymers used in these studies were colloidal stars consisting of a hard dendritic core and a soft polybutadien outer shell. These polymers were dissolved in a solvent squalene and

above the concentration of ~30 weight % macroscopically has properties of a “glass”, however by probing the tracer diffusion at microscopic level using FCS I could show that the tracer and solvent molecules mobility in present system is not affected by this macroscopical “glass transition”.

In the last part of my thesis I demonstrated a new stimuli responsive system based on poly-N-isopropylacrylamide (PNIPAM) and silica inverse opals (iOpals), which are known as a model of porous periodic nanostructures. The interior of the iOpals was modified with PNIPAM brushes via grafting “from” approach using atom transfer radical polymerization (ATRP) method. FCS in this case was applied to study the effect of the temperature on the diffusion of molecular and macromolecular tracers in the iOpal-PNIPAM system. The results, clearly demonstrate that the phase transition of the temperature-responsive polymer can be used to control opening and closing of the grafted iOpal pores and by that we can speed-up or slow-down the mobility of the tracers.

Acknowledgements (are given in printed version)

List of symbols

C	Concentration
c^*	Overlapping concentration
cp^*	Overlapping concentration of probe
D or D_i	Diffusion coefficient of species i
D_0	Diffusion coefficient in pure solvent (at $c = 0$)
D_s	Self diffusion coefficient
$F(t')$	Fluorescence intensity (kHz) at time t'
f_i	Fraction of species i
$G(t)$	Autocorrelation function
G	Gibbs free energy
λ	Wavelength of light
λ_{ex}	Wavelength of excitation light
λ_{em}	Wavelength of emission light
K_B	Boltzmann constant
M_n	Number average molecular weight
M_w	Weight average molecular weight
n	Refractive index
N	Number of monomers in polymer chain
N_A	Avogadro's number
N_p	number of particles in the observation volume
$\langle \Delta r^2(t) \rangle$	Mean square displacement
R_h	Hydrodynamic radius
R_g	Radius of gyration
r_0	Radial axis of confocal volume
S	Structure of parameter ($= z_0/r_0$)
t	Experimental lag time
τ_D	Lateral diffusion time

T	Temperature
T_0	Ideal glass transition temperature
T_g	Glass transition temperature
V	Observation volume
z_0	Vertical axis of confocal volume
η	Viscosity
ξ	Polymer mesh size

List of abbreviations

ATRP	Atom transfer radical polymerization
BP	Band pass transmission filter
DLS	dynamic light scattering
DS	Dielectric spectroscopy
FCS	Fluorescence correlation spectroscopy
FRAP	Fluorescence recovery after photobleaching
FRS	Forced Rayleigh scattering
GPC	Gel Permeation Chromatography
iOpal	Inverse Opal
LP	Long pass transmission filter
LSCM	Laser scanning confocal microscope
MSD	Mean square displacement
NA	Numerical aperture
NMR	Nuclear magnetic resonance
PDI	Perylene-diimide
PDMS	Polydimethylsiloxane
PFG-NMR	Pulsed-field-gradient NMR
PMI	Perylene monoimide
PMT	Photomultiplier
PMPS	Poly(methyl phenyl siloxane)
PNIPAAm	Poly (N-isopropylacrylamide)
PS	Polystyrene
PSF	Point Spread Function
Qdot	Quantum dot
Rh6G	Rhodamine 6G
SE	Stokes-Einstein equation
SEM	Scanning electron microscope
TDI	Terrylene-diimide
THF	Tetrahydrofuran
VD	Vertical deposition

Publications (are given in printed version)

References

1. Fick, A., *Annalen der Physik und Chemie*, 94, 59 (1855). Über Diffusion.
2. Einstein, A., *Ist die Trägheit eines Körpers von seinem Energieinhalt abhängig?* *Annalen der Physik*, 1905. **323**(13): p. 639-641.
3. Chandrasekhar, S. and M. Kac, *Marian Smoluchowski: his life and scientific work*2000: Polish Scientific Publishers PWN Warsaw.
4. Von Smoluchowski, M., *Zur kinetischen theorie der brownischen molekularbewegung und der suspensionen*. *Annalen der Physik*, 1906. **326**(14): p. 756-780.
5. Hänggi, P., P. Talkner, and M. Borkovec, *Reaction-rate theory: fifty years after Kramers*. *Reviews of Modern Physics*, 1990. **62**(2): p. 251.
6. Flynn, C.P. and J.J. Burton, *Point defects and diffusion*. *Physics Today*, 1973. **26**: p. 61.
7. Berne, B.J., *Dynamic light scattering: with applications to chemistry, biology and physics*1976: DoverPublications. com.
8. Andrasko, J., *Water diffusion permeability of human erythrocytes studied by a pulsed gradient NMR technique*. *Biochimica et Biophysica Acta (BBA)-General Subjects*, 1976. **428**(2): p. 304-311.
9. Déléze, J., et al., *Fluorescence recovery after photobleaching*, in *Connexin Methods and Protocols*2001, Springer. p. 313-327.
10. Lumma, D., et al., *Dynamics of large semiflexible chains probed by fluorescence correlation spectroscopy*. *Physical Review Letters*, 2003. **90**(21): p. 218301.
11. DETECTION, S.M., *Fluorescence Correlation Spectroscopy*. *Phys. Rev. Lett*, 1972. **29**: p. 705-708.
12. Rarbach, M., et al., *Dual-color fluorescence cross-correlation spectroscopy for monitoring the kinetics of enzyme-catalyzed reactions*. *Methods*, 2001. **24**(2): p. 104-116.
13. Schwille, P., F. Oehlenschläger, and N.G. Walter, *Quantitative hybridization kinetics of DNA probes to RNA in solution followed by diffusional fluorescence correlation analysis*. *Biochemistry*, 1996. **35**(31): p. 10182-10193.
14. Hausteil, E. and P. Schwille, *Ultrasensitive investigations of biological systems by fluorescence correlation spectroscopy*. *Methods*, 2003. **29**(2): p. 153-166.
15. Cluzel, P., M. Surette, and S. Leibler, *An ultrasensitive bacterial motor revealed by monitoring signaling proteins in single cells*. *Science*, 2000. **287**(5458): p. 1652-1655.
16. Kim, B.-S., et al., *Effect of organic solvent on the permeability and stiffness of polyelectrolyte multilayer microcapsules*. *Macromolecules*, 2005. **38**(12): p. 5214-5222.
17. Zhang, R., et al., *Swelling of cross-linked polystyrene beads in toluene*. *Microelectronic Engineering*, 2008. **85**(5): p. 1261-1264.
18. Vagias, A., et al., *Complex Tracer Diffusion Dynamics in Polymer Solutions*. *Physical Review Letters*, 2013. **111**(8): p. 088301.

19. Raccis, R., et al., *Probing mobility and structural inhomogeneities in grafted hydrogel films by fluorescence correlation spectroscopy*. *Soft Matter*, 2011. **7**(15): p. 7042-7053.
20. Casoli, A. and M. Schönhoff, *Fluorescence correlation spectroscopy as a tool to investigate single molecule probe dynamics in thin polymer films*. *Biological Chemistry*, 2001. **382**(3): p. 363-369.
21. Zettl, H., et al., *Fluorescence correlation spectroscopy of single dye-labeled polymers in organic solvents*. *Macromolecules*, 2004. **37**(5): p. 1917-1920.
22. Grabowski, C.A. and A. Mukhopadhyay, *Diffusion of polystyrene chains and fluorescent dye molecules in semidilute and concentrated polymer solutions*. *Macromolecules*, 2008. **41**(16): p. 6191-6194.
23. Cherdhirankorn, T., et al., *Diffusion in polymer solutions studied by fluorescence correlation spectroscopy*. *The Journal of Physical Chemistry B*, 2009. **113**(11): p. 3355-3359.
24. Cherdhirankorn, T., et al., *Fluorescence correlation spectroscopy study of molecular probe diffusion in polymer melts*. *Macromolecules*, 2009. **42**(13): p. 4858-4866.
25. Cherdhirankorn, T., et al., *Effects of Chain Topology on the Tracer Diffusion in Star Polyisoprenes*. *Macromolecules*, 2009. **42**(22): p. 9183-9189.
26. Doroshenko, M., et al., *Monitoring the Dynamics of Phase Separation in a Polymer Blend by Confocal Imaging and Fluorescence Correlation Spectroscopy*. *Macromolecular rapid communications*, 2012. **33**(18): p. 1568-1573.
27. Minsky, M., *Memoir on inventing the confocal scanning microscope*. *Scanning*, 1988. **10**(4): p. 128-138.
28. Claxton, N.S., T.J. Fellers, and M.W. Davidson, *Laser scanning confocal microscopy*. Olympus. Available online at <http://www.olympusconfocal.com/theory/LSCMIntro.pdf>, 2006.
29. Melet, R., et al. *Resonant emission of a single InAs/GaAs quantum dot in a waveguiding configuration*. in *AIP Conference Proceedings*. 2007.
30. Pawley, J.B., *Handbook of biological confocal microscopy*1995: Springer.
31. Takeuchi, O., et al., *Development of time-resolved scanning tunneling microscopy in femtosecond range*. *Japanese journal of applied physics*, 2002. **41**(part 1): p. 4994-4997.
32. Webb, R.H., *Confocal optical microscopy*. *Reports on Progress in Physics*, 1996. **59**(3): p. 427.
33. Lei, M. and B. Yao, *Characteristics of beam profile of Gaussian beam passing through an axicon*. *Optics communications*, 2004. **239**(4): p. 367-372.
34. Pawley, J.B., *Fundamental limits in confocal microscopy*, in *Handbook of biological confocal microscopy*2006, Springer. p. 20-42.
35. Gordon, G.W., et al., *Quantitative fluorescence resonance energy transfer measurements using fluorescence microscopy*. *Biophysical Journal*, 1998. **74**(5): p. 2702-2713.
36. Chen, H., et al., *The collection, processing, and display of digital three-dimensional images of biological specimens*, in *Handbook of biological confocal microscopy*1995, Springer. p. 197-210.
37. Atkins, P. and J. De Paula, *Atkins' physical chemistry*. Eight Ed, 2006.

38. Song, L., et al., *Influence of the triplet excited state on the photobleaching kinetics of fluorescein in microscopy*. Biophysical Journal, 1996. **70**(6): p. 2959-2968.
39. Wang, X.F., et al., *Fluorescence lifetime imaging microscopy (FLIM): instrumentation and applications*. Critical Reviews in Analytical Chemistry, 1992. **23**(5): p. 369-395.
40. Axelrod, D., et al., *Mobility measurement by analysis of fluorescence photobleaching recovery kinetics*. Biophysical Journal, 1976. **16**(9): p. 1055-1069.
41. Brumbaugh, E.E. and G.K. Ackers, *Molecular sieve studies of interacting protein systems: VII. Direct optical scanning method for ligand-macromolecule binding studies*. Analytical biochemistry, 1971. **41**(2): p. 543-559.
42. Lamola, A.A. and G.S. Hammond, *Mechanisms of photochemical reactions in solution. XXXIII. Intersystem crossing efficiencies*. The Journal of Chemical Physics, 1965. **43**: p. 2129.
43. Lakowicz, J.R., *Excited-State reactions*, in *Principles of Fluorescence Spectroscopy*1999, Springer. p. 515-530.
44. Elson, E.L. and D. Magde, *Fluorescence correlation spectroscopy. I. Conceptual basis and theory*. Biopolymers, 1974. **13**(1): p. 1-27.
45. Thompson, N.L., *Fluorescence correlation spectroscopy*, in *Topics in fluorescence spectroscopy*2002, Springer. p. 337-378.
46. Cherdhirankorn, T., *Diffusion in polymer systems studied by Fluorescence Correlation Spectroscopy*, 2009, Mainz, Univ., Diss., 2009.
47. Rigler, R., *Fluorescence correlations, single molecule detection and large number screening applications in biotechnology*. Journal of biotechnology, 1995. **41**(2): p. 177-186.
48. Schwille, P., *Fluorescence correlation spectroscopy and its potential for intracellular applications*. Cell biochemistry and biophysics, 2001. **34**(3): p. 383-408.
49. Rigler, R. and E.S. Elson, *Fluorescence correlation spectroscopy*2001: Springer.
50. Maiti, S., U. Haupts, and W.W. Webb, *Fluorescence correlation spectroscopy: diagnostics for sparse molecules*. Proceedings of the National Academy of Sciences, 1997. **94**(22): p. 11753-11757.
51. Aragon, S. and R. Pecora, *Fluorescence correlation spectroscopy and Brownian rotational diffusion*. Biopolymers, 1975. **14**(1): p. 119-137.
52. Meseth, U., et al., *Resolution of fluorescence correlation measurements*. Biophysical Journal, 1999. **76**(3): p. 1619-1631.
53. White, J., W. Amos, and M. Fordham, *An evaluation of confocal versus conventional imaging of biological structures by fluorescence light microscopy*. The Journal of cell biology, 1987. **105**(1): p. 41-48.
54. Herrmann, A. and K. Müllen, *From industrial colorants to single photon sources and biolabels: The fascination and function of rylene dyes*. Chemistry Letters, 2006. **35**(9): p. 978.
55. Jung, C., et al., *A new photostable terrylene diimide dye for applications in single molecule studies and membrane labeling*. Journal of the American Chemical Society, 2006. **128**(15): p. 5283-5291.
56. Itakura, M., et al., *Variations in contrast of scanning electron microscope images for microstructure analysis of Si-based semiconductor materials*. Journal of electron microscopy, 2010. **59**(S1): p. S165-S173.

57. Michler, G.H., *Electron microscopy of polymers* 2008: Springer.
58. Davis, K., W. Russel, and W. Glantschnig, *Disorder-to-order transition in settling suspensions of colloidal silica: X-ray measurements*. *Science*, 1989. **245**(4917): p. 507-510.
59. Trau, M., D. Saville, and I. Aksay, *Field-induced layering of colloidal crystals*. *Science*, 1996. **272**(5262): p. 706-709.
60. Jiang, P., et al., *Single-crystal colloidal multilayers of controlled thickness*. *Chemistry of Materials*, 1999. **11**(8): p. 2132-2140.
61. Gu, Z.-Z., A. Fujishima, and O. Sato, *Fabrication of high-quality opal films with controllable thickness*. *Chemistry of Materials*, 2002. **14**(2): p. 760-765.
62. Denkov, N., et al., *Mechanism of formation of two-dimensional crystals from latex particles on substrates*. *Langmuir*, 1992. **8**(12): p. 3183-3190.
63. Fustin, C.-A., et al., *Parameters influencing the templated growth of colloidal crystals on chemically patterned surfaces*. *Langmuir*, 2004. **20**(21): p. 9114-9123.
64. García, P.D., et al., *Photonic glass: a novel random material for light*. *Advanced Materials*, 2007. **19**(18): p. 2597-2602.
65. Still, T., et al., *Simultaneous occurrence of structure-directed and particle-resonance-induced phononic gaps in colloidal films*. *Physical Review Letters*, 2008. **100**(19): p. 194301.
66. Zakhidov, A.A., et al., *Carbon structures with three-dimensional periodicity at optical wavelengths*. *Science*, 1998. **282**(5390): p. 897-901.
67. Milner, S., T. Witten, and M. Cates, *Theory of the grafted polymer brush*. *Macromolecules*, 1988. **21**(8): p. 2610-2619.
68. Advincula, R.C., et al., *Polymer brushes* 2004: Wiley Online Library.
69. Beers, K.L., et al., *The synthesis of densely grafted copolymers by atom transfer radical polymerization*. *Macromolecules*, 1998. **31**(26): p. 9413-9415.
70. Matyjaszewski, K. and J. Xia, *Atom transfer radical polymerization*. *Chemical Reviews*, 2001. **101**(9): p. 2921-2990.
71. Wang, J.-S. and K. Matyjaszewski, *Controlled/"living" radical polymerization. Atom transfer radical polymerization in the presence of transition-metal complexes*. *Journal of the American Chemical Society*, 1995. **117**(20): p. 5614-5615.
72. Grubbs, R.B., *Nitroxide-mediated radical polymerization: limitations and versatility*. *Polymer Reviews*, 2011. **51**(2): p. 104-137.
73. Tsarevsky, N.V., et al., *Copper-based ATRP catalysts of very high activity derived from dimethyl cross-bridged cyclam*. *Journal of Molecular Catalysis A: Chemical*, 2006. **257**(1): p. 132-140.
74. Patten, T.E. and K. Matyjaszewski, *Copper (I)-catalyzed atom transfer radical polymerization*. *Accounts of chemical research*, 1999. **32**(10): p. 895-903.
75. Queffelec, J., S.G. Gaynor, and K. Matyjaszewski, *Optimization of atom transfer radical polymerization using Cu (I)/tris (2-(dimethylamino) ethyl) amine as a catalyst*. *Macromolecules*, 2000. **33**(23): p. 8629-8639.
76. Kistorz, G., *Phase transformations in materials*. *Phase Transformations in Materials*, by Gernot Kistorz (Editor), pp. 724. ISBN 3-527-30256-5. Wiley-VCH, October 2001., 2001. **1**.

77. Koga, T., et al., *Late stage spinodal decomposition in binary fluids: comparison between computer simulation and experimental results*. Physica A: Statistical Mechanics and its Applications, 1993. **198**(3): p. 473-492.
78. Shinozaki, A. and Y. Oono, *Spinodal decomposition in a Hele-Shaw cell*. Physical Review A, 1992. **45**(4): p. R2161.
79. Xie, X.-M., M. Matsuoka, and K. Takemura, *Formation of gradient phase structure during annealing of a polymer blend*. Polymer, 1992. **33**(9): p. 1996-1998.
80. Cahn, J.W., *Phase separation by spinodal decomposition in isotropic systems*. The Journal of Chemical Physics, 1965. **42**: p. 93.
81. Verhoogt, H., et al., *Confocal laser scanning microscopy: a new method for determination of the morphology of polymer blends*. Polymer, 1993. **34**(6): p. 1325-1329.
82. Jinnai, H., et al., *Direct observation of three-dimensional bicontinuous structure developed via spinodal decomposition*. Macromolecules, 1995. **28**(13): p. 4782-4784.
83. Jinnai, H., et al., *Morphological characterization of bicontinuous phase-separated polymer blends and one-phase microemulsions*. Macromolecules, 1997. **30**(1): p. 130-136.
84. López-Barrón, C.R., et al., *Sponge-to-Lamellar Transition in a Double-Tail Cationic Surfactant/Protic Ionic Liquid System: Structural and Rheological Analysis*. The Journal of Physical Chemistry B, 2011. **116**(2): p. 813-822.
85. Crisenza, T., et al., *Direct 3D Visualization of the Phase-Separated Morphology in Chlorinated Polyethylene/Nylon Terpolyamide Based Thermoplastic Elastomers*. Macromolecular rapid communications, 2012. **33**(2): p. 114-119.
86. Bell, J.R., et al., *Annealing of cocontinuous polymer blends: effect of block copolymer molecular weight and architecture*. Macromolecules, 2010. **43**(11): p. 5024-5032.
87. Tran-Cong-Miyata, Q., et al., *Phase separation of polymer mixtures driven by photochemical reactions: Complexity and fascination*. Current Opinion in Solid State and Materials Science, 2011. **15**(6): p. 254-261.
88. Li, L., et al., *Surface morphology of a polymer blend examined by laser confocal fluorescence microscopy*. Langmuir, 1994. **10**(8): p. 2495-2497.
89. Liu, K.L., et al., *A new insight for an old system: protein-PEG colocalization in relation to protein release from PCL/PEG blends*. Molecular pharmaceutics, 2011. **8**(6): p. 2173-2182.
90. Karatasos, K., et al., *Segmental dynamics and incompatibility in hard/soft polymer blends*. The Journal of Chemical Physics, 1998. **108**: p. 5997.
91. Vlassopoulos, D., et al., *Rheology and phase separation in a model upper critical solution temperature polymer blend*. Journal of Rheology, 1997. **41**: p. 739.
92. Gitsas, A., et al., *Effect of Pressure on the Phase Behavior and Segmental Dynamics in Blends of Polystyrene with Poly (methylphenyl siloxane)*. Macromolecules, 2009. **42**(15): p. 5709-5716.
93. Gerharz, B., et al., *Synthesis and characterization of narrowly distributed block copolymers from polystyrene and polymethylphenylsiloxane*. Polymer, 1992. **33**(16): p. 3531-3535.

94. Yamamoto, R. and A. Onuki, *Heterogeneous diffusion in highly supercooled liquids*. Physical Review Letters, 1998. **81**(22): p. 4915.
95. Lipson, J.E., *Studies on fluids and their mixtures using the Born-Green-Yvon integral equation technique*. Macromolecular theory and simulations, 1998. **7**(2): p. 263-282.
96. Wagner, C., *Theory of precipitate change by redissolution*. Z. Electrochem, 1961. **65**(7-8): p. 581-591.
97. Lifshitz, I.M. and V.V. Slyozov, *The kinetics of precipitation from supersaturated solid solutions*. Journal of Physics and Chemistry of Solids, 1961. **19**(1): p. 35-50.
98. White, N.S. and R.J. Errington, *Fluorescence techniques for drug delivery research: theory and practice*. Advanced Drug Delivery Reviews, 2005. **57**(1): p. 17-42.
99. de Gennes, P., *call it "complex fluids," and this does indeed bring in two of the major features:(1) Complexity. We may, in a certain primitive sense*. Reviews of Modern Physics, 1992. **64**(3).
100. Kléman, M. and O.D. Laverntovich, *Soft matter physics: an introduction*2003: Springer.
101. Pusey, P. and W. Van Megen, *Phase behaviour of concentrated suspensions of nearly hard colloidal spheres*. Nature, 1986. **320**(6060): p. 340-342.
102. Cohen, E. and I. De Schepper, *Note on transport processes in dense colloidal suspensions*. Journal of statistical physics, 1991. **63**(1-2): p. 241-248.
103. Brader, J., M. Cates, and M. Fuchs, *First-principles constitutive equation for suspension rheology*. Physical Review Letters, 2008. **101**(13): p. 138301.
104. Siebenbürger, M., et al., *Viscoelasticity and shear flow of concentrated, noncrystallizing colloidal suspensions: Comparison with mode-coupling theory*. Journal of Rheology, 2009. **53**: p. 707.
105. Erwin, B.M., et al., *Dynamics and rheology of colloidal star polymers*. Soft Matter, 2010. **6**(12): p. 2825-2833.
106. Mayer, C., et al., *Asymmetric caging in soft colloidal mixtures*. Nature Materials, 2008. **7**(10): p. 780-784.
107. Rubinstein, M. and A.N. Semenov, *Dynamics of entangled solutions of associating polymers*. Macromolecules, 2001. **34**(4): p. 1058-1068.
108. Gianneli, M., et al., *Local and global dynamics of transient polymer networks and swollen gels anchored on solid surfaces*. The Journal of Physical Chemistry C, 2007. **111**(35): p. 13205-13211.
109. Von Meerwall, E.D., E.J. Amis, and J.D. Ferry, *Self-diffusion in solutions of polystyrene in tetrahydrofuran: Comparison of concentration dependences of the diffusion coefficients of polymer, solvent, and a ternary probe component*. Macromolecules, 1985. **18**(2): p. 260-266.
110. Chekal, B.P. and J.M. Torkelson, *Relationship between chain length and the concentration dependence of polymer and oligomer self-diffusion in solution*. Macromolecules, 2002. **35**(21): p. 8126-8138.
111. Gu, Z.Z., et al., *Infiltration of colloidal crystal with nanoparticles using capillary forces: a simple technique for the fabrication of films with an ordered porous structure*. Applied Physics a-Materials Science & Processing, 2002. **74**(1): p. 127-129.

112. Li, Q., et al., *Porous Networks Through Colloidal Templates*, in *Templates in Chemistry III*, P. Broekmann, K.H. Dotz, and C.A. Schalley, Editors. 2009, Springer-Verlag Berlin: Berlin. p. 135-180.
113. Wang, J., et al., *Structural and optical characterization of 3D binary colloidal crystal and inverse opal films prepared by direct co-deposition*. *Journal of Materials Chemistry*, 2008. **18**(9): p. 981-988.
114. Wang, J.J., et al., *Preparation of multilayered trimodal colloid crystals and binary inverse opals*. *Journal of the American Chemical Society*, 2006. **128**(49): p. 15606-15607.
115. Nykypanchuk, D., H.H. Strey, and D.A. Hoagland, *Brownian motion of DNA confined within a two-dimensional array*. *Science*, 2002. **297**(5583): p. 987-990.
116. Heskins, M. and J.E. Guillet, *Solution properties of poly (N-isopropylacrylamide)*. *Journal of Macromolecular Science—Chemistry*, 1968. **2**(8): p. 1441-1455.
117. You, Y.Z., et al., *Temperature-controlled uptake and release in PNIPAM-modified porous silica nanoparticles*. *Chemistry of Materials*, 2008. **20**(10): p. 3354-3359.
118. Vasani, R.B., et al., *Stimulus-Responsiveness and Drug Release from Porous Silicon Films ATRP-Grafted with Poly(N-isopropylacrylamide)*. *Langmuir*, 2011. **27**(12): p. 7843-7853.
119. Ramakrishnan, A., R. Dhamodharan, and J. Rühle, *Controlled growth of PMMA brushes on silicon surfaces at room temperature*. *Macromolecular rapid communications*, 2002. **23**(10-11): p. 612-616.
120. Cherdhirankorn, T., et al., *Tracer diffusion in silica inverse opals*. *Langmuir*, 2010. **26**(12): p. 10141-10146.
121. Enderlein, J., et al., *Art and artefacts of fluorescence correlation spectroscopy*. *Current pharmaceutical biotechnology*, 2004. **5**(2): p. 155-161.
122. Wang, J., et al., *Preparation of multilayered trimodal colloid crystals and binary inverse opals*. *Journal of the American Chemical Society*, 2006. **128**(49): p. 15606-15607.
123. Raccis, R., et al., *Confined Diffusion in Periodic Porous Nanostructures*. *Acs Nano*, 2011. **5**(6): p. 4607-4616.

Curriculum Vitae (is given in printed version)

